Chinese Journal of Natural Medicines

Evaluation of pharmacokinetics and metabolism of three marine-derived piericidins for guiding drug lead selection

Weimin Liang, Jindi Lu, Ping Yu, Meiqun Cai, Danni Xie, Xini Chen, Xi Zhang, Lingmin Tian, Liyan Yan, Wenxun Lan, Zhongqiu Liu, Xuefeng Zhou, Lan Tang

Citation: Weimin Liang, Jindi Lu, Ping Yu, Meiqun Cai, Danni Xie, Xini Chen, Xi Zhang, Lingmin Tian, Liyan Yan, Wenxun Lan, Zhongqiu Liu, Xuefeng Zhou, Lan Tang, Evaluation of pharmacokinetics and metabolism of three marine-derived piericidins for guiding drug lead selection, Chinese Journal of Natural Medicines, 2025, 23(5), 614-629. doi: 10.1016/S1875-5364(25)60866-1.

View online: https://doi.org/10.1016/S1875-5364(25)60866-1

Chinese Journal of Natural Medicines 23 (2025) 614-629

Contents lists available at ScienceDirect

Chinese Journal of Natural Medicines

journal homepage: www.cjnmcpu.com/

Original article

Evaluation of pharmacokinetics and metabolism of three marine-derived piericidins for guiding drug lead selection

Weimin Liang[a,Δ], Jindi Lu[a,Δ], Ping Yu[a], Meiqun Cai[a], Danni Xie[a], Xini Chen[a], Xi Zhang[a], Lingmin Tian[a], Liyan Yan[a], Wenxun Lan[a], Zhongqiu Liu[c], Xuefeng Zhou[b,*], Lan Tang[a,*]

[a] *NMPA Key Laboratory for Research and Evaluation of Drug Metabolism & Guangdong Provincial Key Laboratory of New Drug Screening & Guangdong-Hongkong-Macao Joint Laboratory for New Drug Screening, School of Pharmaceutical Sciences, Southern Medical University, Guangzhou 510515 China*

[b] *CAS Key Laboratory of Tropical Marine Bio-resources and Ecology/Guangdong Key Laboratory of Marine Materia Medica, South China Sea Institute of Oceanology, Chinese Academy of Sciences, Guangzhou 510301, China*

[c] *International Institute for Translational Chinese Medicine, Guangzhou University of Chinese Medicine, Guangzhou 510006, China*

ARTICLE INFO

Article history:
Received 12 September 2024
Revised 25 December 2024
Accepted 30 December 2024
Available online 20 May 2025

Keywords:
Piericidin glycosides
Pharmacokinetics
Metabolism
Drug evaluation
Drug lead selection

ABSTRACT

This study investigates the pharmacokinetics and metabolic characteristics of three marine-derived piericidins as potential drug leads for kidney disease: piericidin A (PA) and its two glycosides (GPAs), glucopiericidin A (GPA) and 13-hydroxyglucopiericidin A (13-OH-GPA). The research aims to facilitate lead selection and optimization for developing a viable preclinical candidate. Rapid absorption of PA and GPAs in mice was observed, characterized by short half-lives and low bioavailability. Glycosides and hydroxyl groups significantly enhanced the absorption rate (13-OH-GPA > GPA > PA). PA and GPAs exhibited metabolic instability in liver microsomes due to Cytochrome P450 enzymes (CYPs) and uridine diphosphoglucuronosyl transferases (UGTs). Glucuronidation emerged as the primary metabolic pathway, with UGT1A7, UGT1A8, UGT1A9, and UGT1A10 demonstrating high elimination rates (30%–70%) for PA and GPAs. This rapid glucuronidation may contribute to the low bioavailability of GPAs. Despite its low bioavailability (2.69%), 13-OH-GPA showed higher kidney distribution (19.8%) compared to PA (10.0%) and GPA (7.3%), suggesting enhanced biological efficacy in kidney diseases. Modifying the C-13 hydroxyl group appears to be a promising approach to improve bioavailability. In conclusion, this study provides valuable metabolic insights for the development and optimization of marine-derived piericidins as potential drug leads for kidney disease.

1. Introduction

The significance of marine natural products (MNPs) in drug discovery has been extensively documented. As of 2023, over 40 000 MNPs have been identified, with more than half demonstrating various biological activities or medicinal potential. Through collaboration with pharmacologists, the number of reported drug leads from marine sources is increasing, indicating a promising trend in marine drug research [1]. However, it is important to note that the number of marine-derived drug candidates in clinical and preclinical pipelines remains limited, despite high expectations [2]. Consequently, the careful selection and optimization of lead compounds for developing promising preclinical candidates is crucial in advancing marine drug research and development.

Our comprehensive research on marine-derived natural piericidins and their medicinal potential has yielded significant results. We obtained and identified forty-three natural piericidins, including twenty piericidin glycosides, from two marine-derived actinomycete strains. Notably, twenty-nine of these compounds were reported as novel by our team [3-5]. Activity screening and pharmacological studies have indicated that several piericidin derivatives, both glycosides and aglycones, show promise for kidney disease treatment. The majority of piericidins exhibited substantial cytotoxicity against three renal carcinoma cell lines: ACHN, OS-RC-2, and 786-O. Some compounds, such as piericidin A (PA), glucopiericidin A (GPA), and 13-hydroxyglucopiericidin A (13-OH-GPA), demonstrated selective activity towards ACHN. PA and its glycosides (GPAs) were found to induce cell apoptosis by reducing reactive oxygen species levels, a process mediated by upregulated PRDX1 mRNA and protein levels. These compounds also demonstrated potent antitumor efficacy in nude mice bearing ACHN xenografts [5]. 13-OH-GPA, characterized by low toxicity, showed the ability to retard renal fibrosis and acute kidney injury (AKI) by promoting autophagy and mitochondrial homeostasis, acting as a novel liver kinase B1 (LKB1) activator [6]. Our research further elucidated the mechanism of hepatotoxicity under high cholesterol conditions caused by piericidins *in vivo* and *in vitro*, highlighting a notable difference between the glycoside (GPA) and aglycone (PA) forms [7]. These findings suggest that PA and GPAs (GPA and 13-OH-GPA), as potential drug leads for kidney disease, could offer innovative therapeutic approaches for

* Corresponding author.
E-mail addresses: xfzhou@scsio.ac.cn (X. Zhou); tl405@smu.edu.cn (L. Tang)
Δ These authors contributed equally to this work.

https://doi.org/10.1016/S1875-5364(25)60866-1

kidney cancer or chronic kidney disease. However, further investigation is required to fully understand how structural differences in piericidins, such as glycosylation and hydroxyl substitution, affect their druggability.

To advance piericidin derivatives as potential therapeutic agents for kidney disease prevention and treatment, it is essential to identify a lead compound with optimal druggability for further investigation. This process encompasses large-scale preparation and comprehensive preclinical studies. The selection of a lead compound should not only focus on drug efficacy but also enhance absorption, distribution, metabolism, excretion, and toxicity (ADME/T) profiles, as well as improve the chemical accessibility associated with natural leads [8].

Characterizing the ADME/T properties of novel candidate drugs is essential for successful drug development [9, 10]. Metabolic biotransformation of drugs can reduce their half-life, expedite drug elimination, and significantly impact efficacy and safety [11]. Utilizing an *in vitro* hepatic microsomal incubation system to screen the metabolic stability of drug candidates facilitates understanding their susceptibility to biotransformation [11]. Moreover, identifying metabolites through high-resolution mass spectrometry (HRMS) analysis can elucidate the metabolic transformation pathways and reaction types of drug candidates [12–14]. Cytochrome P450 enzymes (CYPs) are involved in the Phase I metabolism of approximately 50% of clinically used drugs, and their activity directly influences the biotransformation and metabolism of multiple drugs [15]. In experimental research, a cocktail approach employing multiple probe drugs is frequently used to efficiently evaluate the impact of drugs on various CYP activities, enabling assessment of potential drug-drug interactions (DDIs) of drug candidates [16].

This study aims to comprehensively elucidate the pharmacokinetic behavior and metabolic characteristics of three marine-derived piericidins (PA, GPA, and 13-OH-GPA, Fig. 1) as potential drug leads for kidney disease. It emphasizes the correlation between chemical structure and drug properties, establishing a comprehensive drug evaluation system. This approach is crucial for elucidating the relationship between structure and efficacy, thereby advancing the development of natural piericidins as potential candidates for the treatment of nephropathy.

2. Results

2.1. Pharmacokinetics

To compare the *in vivo* processes following the administration of PA and GPAs, pharmacokinetic experiments were conducted in mice using both oral and tail vein administration routes (Figs. 2A-2F). The pharmacokinetic parameters derived from the data were calculated and expressed as mean ± standard deviation, as presented in Table 1.

The pharmacokinetic profiles revealed that the area under the plasma concentration-time curve ($AUC_{0\text{-}t}$) for PA/GPA/13-OH-GPA was 1679.499 ± 184.558, 3023.653 ± 561.785, and 2896.599 ± 287.906 μg/L*min, respectively, following oral administration. The time to reach peak concentration (T_{max}) for PA, GPA, and 13-OH-GPA was 30, 10, and 2 min, indicating rapid absorption into the circulatory system with absorption rates in the order of 13-OH-GPA > GPA > PA. After reaching peak concentrations, PA, GPA, and 13-OH-GPA were swiftly eliminated from plasma, demonstrating rapid clearance (CL) of 3.232 ± 0.393, 3.323 ± 0.598, and 3.384 ± 0.382 $L{\cdot}min^{-1}{\cdot}kg^{-1}$, and short half-lives ($T_{1/2}$) of 25.06 ± 8.304, 19.034 ± 6.063, and 22.551 ± 10.539 min, respectively. Moreover, the mean residence time ($MRT_{0\text{-}t}$) of GPA and 13-OH-GPA was shorter than that of PA. All drugs were effectively eliminated within 100–150 min post-administration, falling below the detection limit.

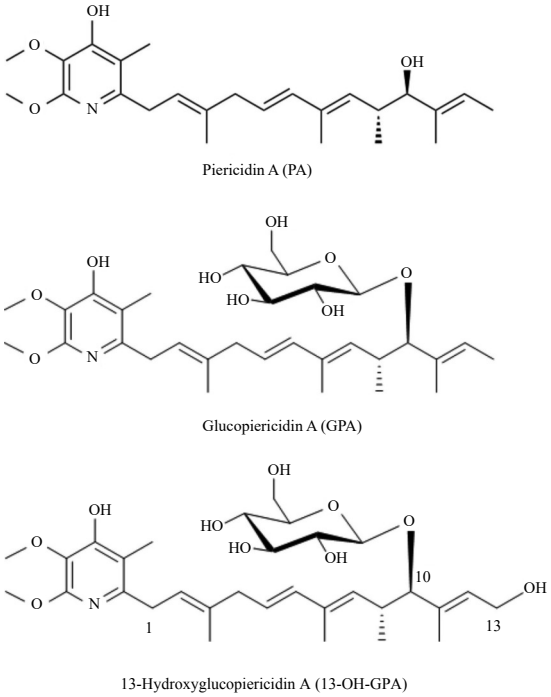

Fig. 1 Structure of the three marine-derived drug candidates.

According to the literature reports, the LD_{50} values for mice treated with intravenous PA injection were < 1.0 $mg{\cdot}kg^{-1}$ [17]. When administered a tail vein dose of 0.8 $mg{\cdot}kg^{-1}$, mice survived until the experiment's conclusion. Due to the low dose, pharmacokinetic profiles could only be collected for the initial 15 minutes, preventing the acquisition of relevant pharmacokinetic parameters. Consequently, this study focused on comparing the *in vivo* behavior of tail vein administration of GPA (2 $mg{\cdot}kg^{-1}$) and 13-OH-GPA (2 $mg{\cdot}kg^{-1}$) in mice. Both GPA and 13-OH-GPA were rapidly eliminated from plasma after tail vein injection, but their clearance rates differed. The $T_{1/2}$ of 13-OH-GPA (27.374 ± 6.041 min) was shorter than that of GPA (48.201 ± 12.037 min). Additionally, the CL of 13-OH-GPA (0.92 ± 0.07 $L{\cdot}min^{-1}{\cdot}kg^{-1}$) was approximately six times that of GPA (0.154 ± 0.017 $L{\cdot}min^{-1}{\cdot}kg^{-1}$). These parameters indicate that 13-OH-GPA was eliminated from plasma more rapidly than GPA following tail vein administration. Furthermore, the calculated absolute bioavailability (F%) of GPA and 13-OH-GPA was extremely low, at 5.06% and 2.69%, respectively.

2.2. Distribution

The concentrations of PA, GPA, and 13-OH-GPA in the primary tissues of mice following gastric administration are presented in Figs. 2G–2I. The tissue distribution proportion is illustrated in Fig. 2J. The drugs were distributed across all examined tissues in the mice. The tissue distribution order for PA was liver > kidney > heart> lung > spleen, corresponding to 79.0%, 10.0%, 7.6%, 1.9%, and 1.4%, respectively. For GPA, the order was liver > lung > heart > spleen > kidney, corresponding to 50.2%, 22.9%, 11.0%, 8.6%, and 7.3%. The distribution order for 13-OH-GPA was liver > kidney > heart > lung > spleen, corresponding to 55.7%, 19.8%, 11.5%, 7.6%, and 5.3%. The distribution results indicated that post-administration, a significant proportion of the drugs concentrated in the liver, particularly PA, with nearly 80% of the drug proportion, followed by kidney, lung, heart, and spleen. Among the three drugs, excluding the liver, GPA showed the highest proportion in the lung, while 13-OH-GPA had the largest proportion in the kidney. Additionally, PA was de-

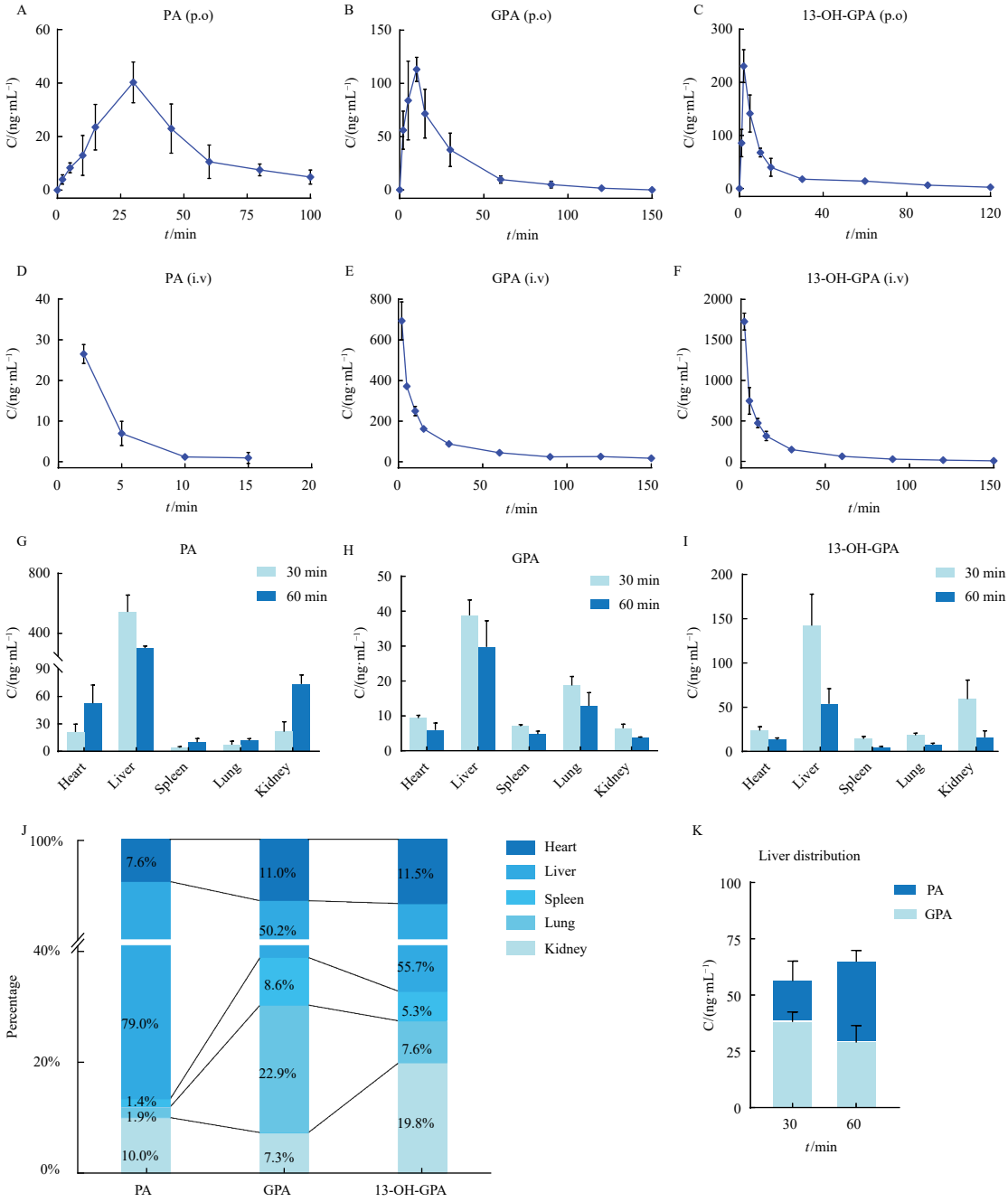

Fig. 2 Plasma concentration-time profile and tissue distribution plots after PA/GPA/13-OH-GPA administration in mice. The data are expressed as mean ± SD (n = 5). (A–C) Plasma concentration-time curves for PA (6 mg·kg^{-1}), GPA (10 mg·kg^{-1}), and 13-OH-GPA (10 mg·kg^{-1}) after oral administration. (D–F) Plasma concentration-time curves for PA (0.8 mg·kg^{-1}), GPA (2 mg·kg^{-1}), and 13-OH-GPA (2 mg·kg^{-1}) after intravenous administration. (G–I) Drug concentrations in each tissue in mice at 30 min and 60 min for PA, GPA and 13-OH-GPA after oral administration. (J) Proportion (%) of PA/GPA/13-OH-GPA distribution in each tissue. Percentages in the figure are the mean of the proportion of the tissue distribution at two time points. (K) Amount of GPA and PA in the liver after GPA administration.

tected in the liver following GPA administration (Fig. 2K), consistent with previously reported findings [7]. Over time, GPA was converted to PA in the liver through the removal of glycoside groups post-administration. However, this biotransformation was not observed in the other four tissues or plasma.

2.3. Identification of CYP metabolites in rat liver microsomes (RLMs) and human liver microsomes (HLMs)

The total ion flow chromatograms and metabolic pathways of 10 μmol·L^{-1} PA, GPA, and 13-OH-GPA after 60 min incubation in RLMs and HLMs containing nicotinamide adenine dinucleotide phosphate (NADPH) are presented in Fig. 3. The primary MS2 spectra are illustrated in Figs. 4, while the MS2 spectra of all CYP metabolites are provided in the supporting information (Figs. S1–S3). Metabolites were identifiedt through analysis of chromatographic behavior and ass spectral fragmentation patterns. Table 2 summarizes the retention times and relevant mass spectral information used for identification.

2.3.1. PA and its CYP metabolites

Eight CYP-mediated metabolites (M1–M8) were identified in RLMs, whereas only four CYP-mediated metabolites (M2, M6, M7, M8) were detected in HLMs (Fig. 3A). This observation demonstrates significant inter-species variability in CYP-mediated metabolism of PA in microsomes. The proposed metabolic pathways are illustrated in Fig. 3B.

In the positive ion mode, the elution peak at 20.2 min corres-

Table 1 Main pharmacokinetic parameters of PA/GPA/13-OH-GPA in mice after oral and tail vein administration. The data are expressed as mean ± SD (n = 5). $^{****}P < 0.001$ *vs* PA group; $^{\#\#}P < 0.01$, $^{\#\#\#}P < 0.005$, $^{\#\#\#\#}P < 0.001$ *vs* GPA group.

Parameter	PA (p.o 6 mg·kg^{-1})	GPA (p.o 10 mg·kg^{-1})	13-OH-GPA (p.o 10 mg·kg^{-1})
$AUC_{0\text{-}t}$ (μg/L*min)	1679.499 ± 184.558	3023.653 ± 561.785	2896.599 ± 287.906
$AUC_{0\text{-}\infty}$ (μg/L*min)	1877.105 ± 213.209	3090.541 ± 572.033	2983.836 ± 325.973
$MRT_{0\text{-}t}$ (min)	39.481 ± 1.674	24.388 ± 3.441****	25.002 ± 3.142****
$T_{1/2}$ (min)	25.06 ± 8.304	19.034 ± 6.063	22.551 ± 10.539
T_{max} (min)	30 ± 0	10 ± 0	2 ± 0
CL (L/min/kg)	3.232 ± 0.393	3.323 ± 0.598	3.384 ± 0.382
C_{max} (μg/L)	40.283 ± 7.622	113.232 ± 11.392	230.619 ± 31.026
Parameter	PA (i.v 0.8 mg·kg^{-1})	GPA (i.v 2 mg·kg^{-1})	13-OH-GPA (i.v 2 mg·kg^{-1})
$AUC_{0\text{-}t}$ (μg/L*min)	-	11957.283 ± 744.242	21526.654 ± 1769.188$^{\#\#\#\#}$
$AUC_{0\text{-}\infty}$ (μg/L*min)	-	13149.272 ± 1446.485	21827.284 ± 1714.284$^{\#\#\#\#}$
$MRT_{0\text{-}t}$ (min)	-	31.985 ± 3.282	21.463 ± 2.355$^{\#\#\#}$
$T_{1/2}$ (min)	-	48.201 ± 12.037	27.374 ± 6.041$^{\#\#}$
CL (L/min/kg)	-	0.154 ± 0.017	0.92 ± 0.07$^{\#\#\#\#}$
Bioavailability (F%)	-	5.06	2.69

ponded to unmodified PA (*m/z* 416.2787, confirmed as $C_{25}H_{37}NO_4 + H^+$). The MS2 spectrum of the protonated molecular ion $[M + H]^+$ yielded four characteristic fragment ions at *m/z* 398, 332, 208, and 182, which provided valuable fragmentation information for metabolite identification.

M1 (*m/z* 448.2667, confirmed as $C_{25}H_{37}NO_6 + H^+$) exhibited a retention time of 11 min. The protonated molecular ion $[M + H]^+$ was 32 Da (2O) greater than PA, and the diagnostic ions at *m/z* 430 were 32 Da higher than fragment ions at *m/z* 398 of PA, indicating that M1 was a dioxygenated metabolite of PA.

The retention times of metabolites M2–M7 (*m/z* 432.2722, 432.2719, 432.2786, 432.2709, 432.2758, and 432.2725, confirmed as $C_{25}H_{37}NO_5 + H^+$) were 14.9, 15.5, 15.9, 16.5, 17.2, and 17.9 min, respectively. The protonated molecular ion $[M + H]^+$ exhibited a 16 Da (O) increase compared to PA, and the fragment ions at *m/z* 414 were 16 Da higher than the fragmentation ions at *m/z* 398 of PA, indicating that these were monooxygenated metabolites of PA. Metabolites M2–M7 were determined to be isomers of each other, with varying oxidation sites. Considering the biosynthetic effects and structural characteristics, potential oxidation types include hydroxylation, epoxidation, and N-oxidation of the pyridine ring, with hydroxylation being the most probable. Due to the multiple potential oxidation sites within the structure, the precise location of the mono-/di-oxygenated metabolites could not be definitively characterized.

M8 (*m/z* 414.2635, confirmed as $C_{25}H_{35}NO_4 + H^+$) exhibited a retention time of 20.6 min, with its $[M + H]^+$ ion being 2 Da (2H) lower than PA. Consequently, M8 was identified as a dehydrogenated metabolite of PA. Based on structural characteristics, it was hypothesized that a hydroxyl group attached to C-10 undergoes dehydrogenation, transforming into a carbonyl group, thus forming metabolite M8.

2.3.2. GPA and its CYP metabolites

GPA demonstrated notable species-specific differences in CYP-mediated metabolism within the microsomes. Eight GPA M1-M8 were identified in RLMs, while three GPA metabolites (M6-M8) were detected in HLMs (Fig. 3C). The proposed metabolic pathways are illustrated in Fig. 3D.

The chromatographic peak with a retention time of 14.8 min was identified as GPA (*m/z* 578.3339, confirmed as $C_{31}H_{47}NO_9 + H^+$). The MS2 spectrum of GPA revealed that GPA initially underwent glycoside removal (162 Da), forming the fragment ion *m/z* 416 (PA). Subsequently, fragment ions *m/z* 398, 332, and 182 were produced, which closely corresponded to the primary fragment ions of PA.

Analysis of metabolite chromatographic behavior and mass spectrometry data revealed that GPA underwent metabolic reactions similar to PA in CYP-mediated metabolism in microsomes. Five dioxygenated metabolites (M1–M5, *m/z* 610.3245, 610.3240, 610.3274, 610.3283, 610.3183, confirmed as $C_{31}H_{47}NO_{11} + H^+$), two monooxygenated metabolites (M6 and M8, *m/z* 594.3309, 594.3325, confirmed as $C_{31}H_{47}NO_{10} + H^+$) and one dehydrogenated metabolite (M7, *m/z* 576.3189, confirmed as $C_{31}H_{45}NO_9 + H^+$)were identified. Fragment ions (*m/z* 448, 430) from M1-M5, fragment ions (*m/z* 432, 414) from M6 and M8, and fragment ions (*m/z* 414, 396) from M7 were 32 Da more, 16 Da more, and 2 Da less than those (*m/z* 416, 398) from GPA, respectively. These fragments provided evidence for metabolite identification. For the dehydrogenated metabolite M7, it is hypothesized that two hydrogen molecules were removed, forming a double bond between C-9 and C-15, resulting in M7 formation.

Additionally, metabolite M6 exhibited an identical chromatographic retention time and a highly consistent MS2 spectrum compared to 13-OH-GPA. The relative abundance of their secondary fragment ions also demonstrated similarity (Figs. S4). Given that GPA and 13-OH-GPA differ structurally by only one hydroxyl group and 16 Da in molecular weight, it is reasonable to infer that M6 is likely 13-OH-GPA. This suggests that the biotransformation of GPA to 13-OH-GPA may occur within liver microsomes. However, further confirmation of this conclusion is necessary.

2.3.3. 13-OH-GPA and its CYP metabolites

Five metabolites (M1–M4, M6) and six metabolites (M1–M6) of 13-OH-GPA were identified in RLMs and HLMs, respectively (Fig. 3E). The proposed metabolic pathways are illustrated in Fig. 3F.

The peak with a retention time of 11.6 min was identified as 13-OH-GPA (*m/z* 594.3316, confirmed as $C_{31}H_{47}NO_{10} + H^+$) exhibiting characteristic fragment ions at *m/z* 432, 414, 396 and 330.

The retention times for metabolites M1, M3, M4, and M5 (*m/z* 610.3283, 610.3246, 610.3194, 610.3236, confirmed as $C_{31}H_{47}NO_{11} + H^+$) were observed at 9.0, 9.9, 10.2, and 11.0 min, respectively. Their molecular ions $[M + H]^+$ exhibited a mass increase of 16 Da compared to 13-OH-GPA. The MS2 profile re-

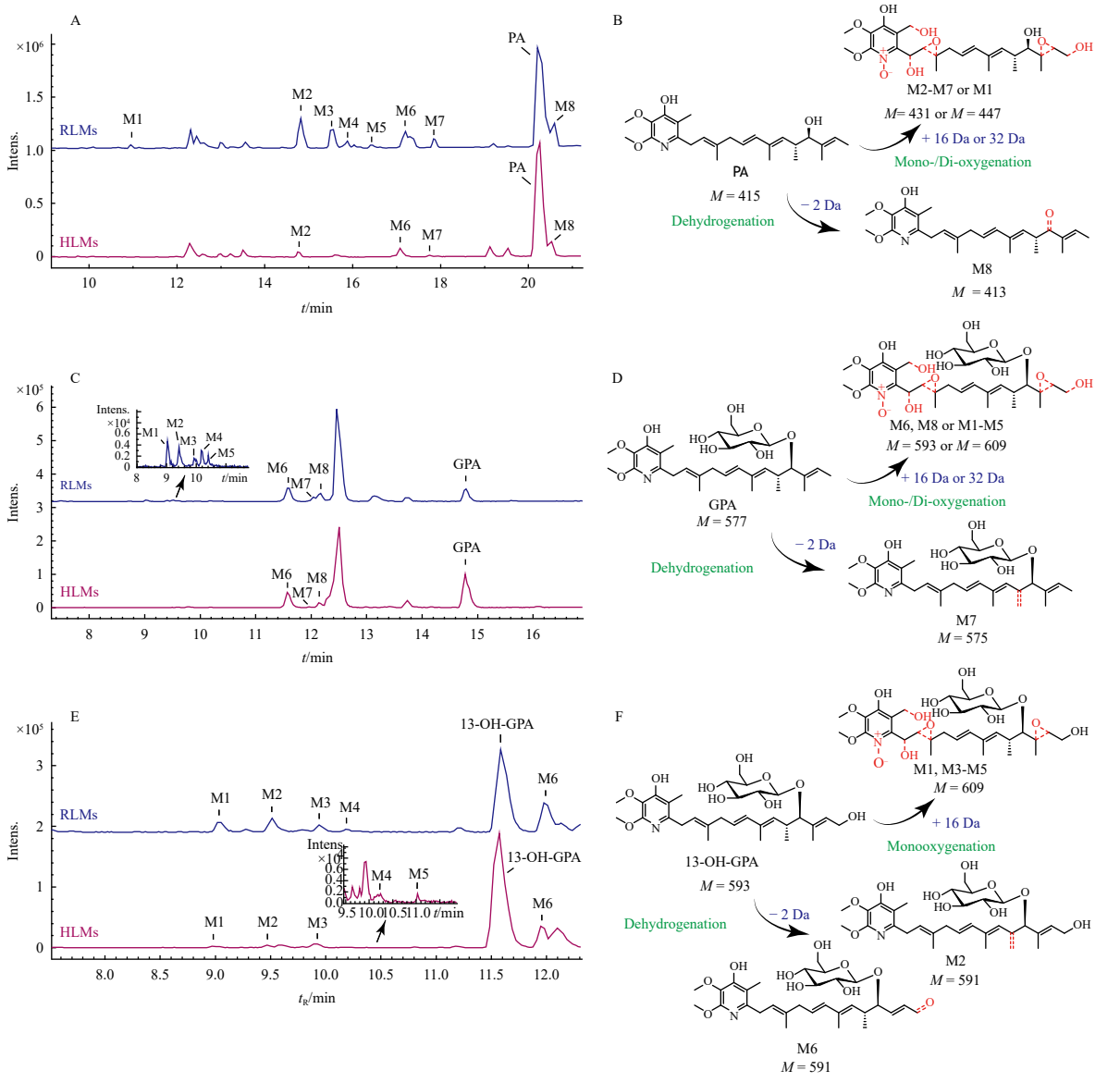

Fig. 3 Identification of the CYP metabolites of PA/GPA/13-OH-GPA in RLMs and HLMs. (A–B) Total ion flow chromatograms of PA (10 μmol·L^{-1}) after CYPs-mediated metabolism in microsomes and the proposed metabolic pathways. Eight CYP metabolites of PA (M1–M8) were identified in RLMs, and four CYP metabolites of PA (M2, M6, M7, M8) were identified in HLMs. (C–D) Total ion flow chromatograms of GPA (10 μmol·L^{-1}) after CYPs-mediated metabolism in microsomes and the proposed metabolic pathways. Eight CYP metabolites of GPA (M1–M8) were identified in RLMs, and three CYP metabolites of GPA (M6–M8) were identified in HLMs. (E–F) Total ion flow chromatograms of 13-OH-GPA (10 μmol·L^{-1}) after CYPs-mediated metabolism in microsomes and the proposed metabolic pathways. Five CYP metabolites of 13-OH-GPA (M1–M4, M6) were identified in RLMs, and six CYP metabolites of 13-OH-GPA (M1–M6) were identified in HLMs.

vealed fragment ions at *m/z* 448 and 412, which were 16 Da higher than the fragment ions at *m/z* 432 and 396 of 13-OH-GPA, respectively. This evidence suggests that these metabolites are monooxygenated derivatives of 13-OH-GPA.

The retention times of M2 and M6 (*m/z* 592.3147, 592.3155, confirmed as $C_{31}H_{45}NO_{10}$ + H^+) were 9.5 min and 12.0 min. The molecular ions $[M + H]^+$ exhibited a mass 2 Da less than that of 13-OH-GPA, and the fragment ions at *m/z* 430 and 412 observed in the mass spectra were also 2 Da less than those of 13-OH-GPA. Consequently, M2 and M6 were identified as dehydrogenation products of 13-OH-GPA. Regarding the dehydrogenation site, it was highly probable that either the hydroxyl group at C-13 transformed into a carbonyl group or a double bond formed between C-9 and C-15.

2.4. Identification of uridine diphosphoglucuronosyl transferase (UGT) metabolites in RLMs and HLMs

PA, GPA, and 13-OH-GPA demonstrate notable species-specific differences in UGT-mediated metabolism. Each compound produced a single metabolite in RLMs, while HLMs generated one to two metabolites (Figs. 5A–5C). Analysis of fragment ion information revealed that the molecular ion peaks of the five metabolites were all 176 Da higher than their respective prototypes, indicating that these products were all monoglucuronide metabolites. Considering steric hindrance and electronic effects, the glucuronide was likely added to the hydroxyl groups at C-4', C-10 (for PA), or C-13 (for 13-OH-GPA). Figs. 5D–5F illustrate the proposed chemical structures of the monoglucuronide metabolites, while Figs. 6A–6C present the corresponding MS2 spectra. Table 2 summarizes the relevant identification information of metabolites. Fig. 7 provides an overview of the metabolic pathways mediated by CYPs and UGTs for PA, GPA, and 13-OH-GPA.

2.5. CYP- and UGT-mediated metabolism

The metabolic stability of CYPs and UGTs was investigated using a consistent concentration of HLMs (Figs. 8A–8C). PA, GPA, and 13-OH-GPA demonstrated rapid elimination and metabolic instability in both CYP and UGT reactions during 15, 30, and 60-

minute incubation periods. After 60 minutes, the remaining percentages of PA, GPA, and 13-OH-GPA in the CYP reactions were 39.25%, 13.68%, and 60.80%, respectively. In contrast, the remaining percentages in the glucuronidation reactions were 14.19%, 0.00%, and 5.38%, respectively. The higher remaining percentages in the CYP reactions compared to the UGT reactions suggest that glucuronidation reactions occurred significantly faster than CYP reactions. Consequently, PA and GPAs were predominantly metabolized through glucuronidation rather than CYP-mediated reactions. Additionally, the natural log curve of the residue percentage (LN%) was plotted based on *in vitro* to *in vivo* extrapolation (IVIVE) (Figs. 8D–8F) [18, 19]. In the CYP assay, the *in vivo* CL_{int} values for PA, GPA, and 13-OH-GPA were 12.62, 5.46, and 13.50 $mL \cdot min^{-1} \cdot kg^{-1}$, respectively. In the UGT assay, the *in vivo* CL_{int} values for PA, GPA, and 13-OH-GPA were 42.42, 32.04, and 34.43 $mL \cdot min^{-1} \cdot kg^{-1}$, respectively. These results further indicate that PA and GPAs exhibited faster liver elimination rates under UGT-mediated metabolism.

To characterize the CYP and UGT isoforms responsible for the metabolism of PA, GPA, and 13-OH-GPA, these compounds were incubated with eight recombinant human CYPs and twelve recombinant human UGTs to assess the metabolism of each enzyme based on the prototype elimination rate. The results indicated that all eight CYPs were involved in the metabolism of PA, GPA, and 13-OH-GPA to varying degrees, with prototype elimination rates below 20% for all (Figs. 9A–9C). PA and GPA exhibited no significant metabolic differences across the CYPs. The prototype elimination rate of 13-OH-GPA in CYP1A2 and CYP2A9 was

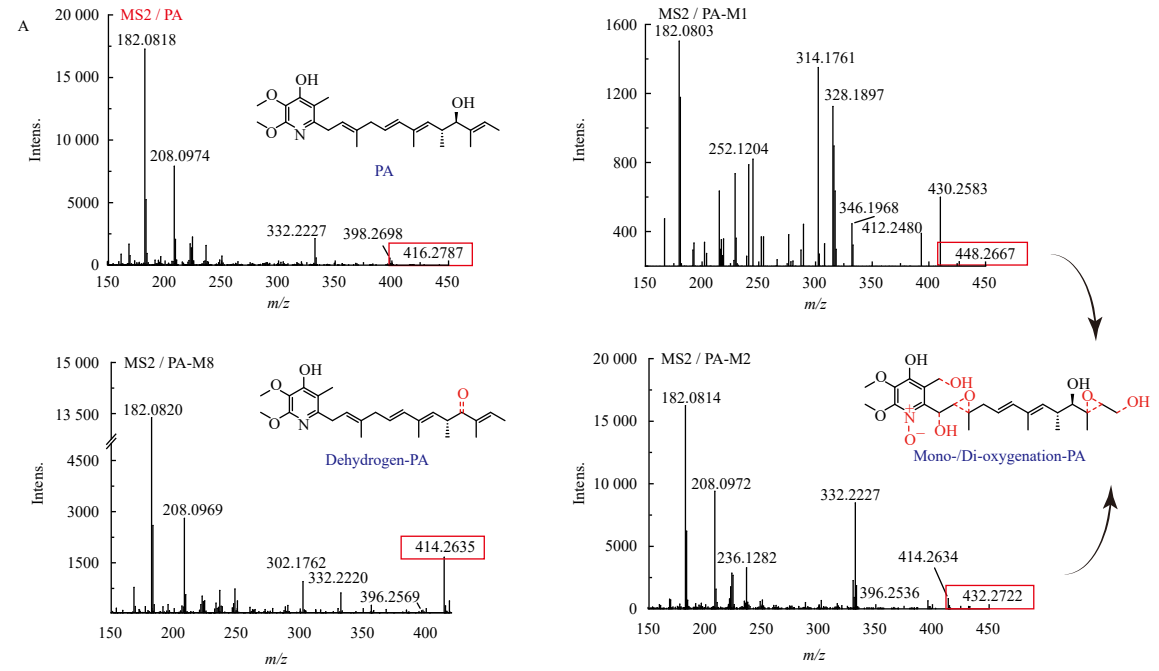

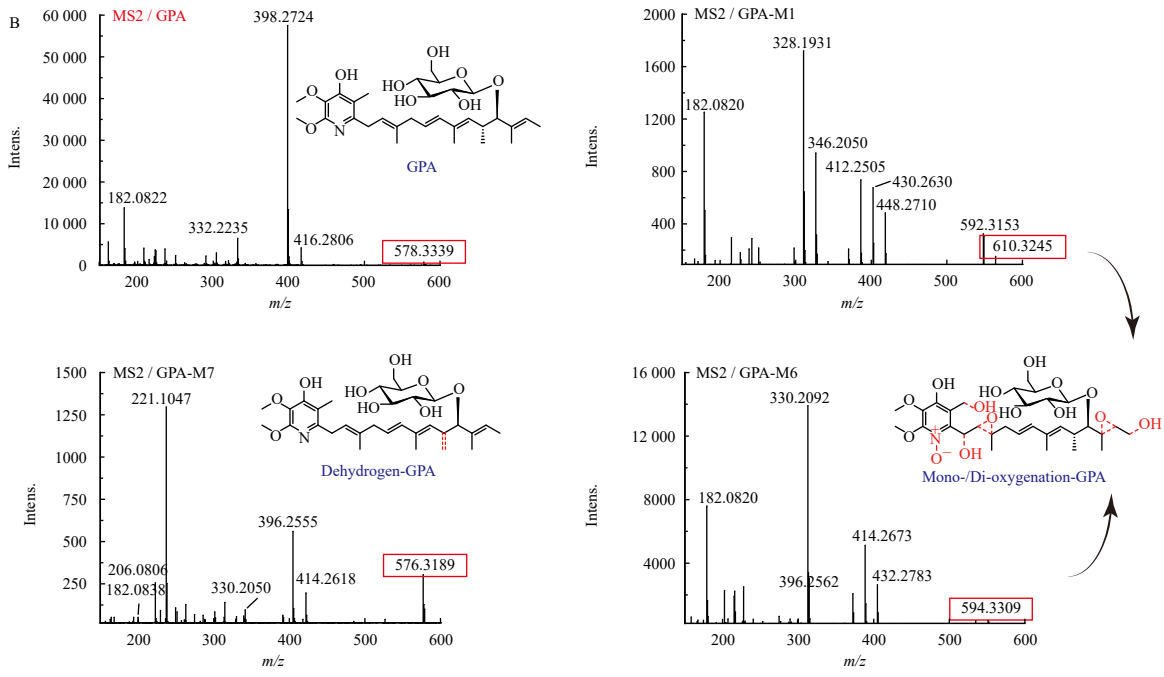

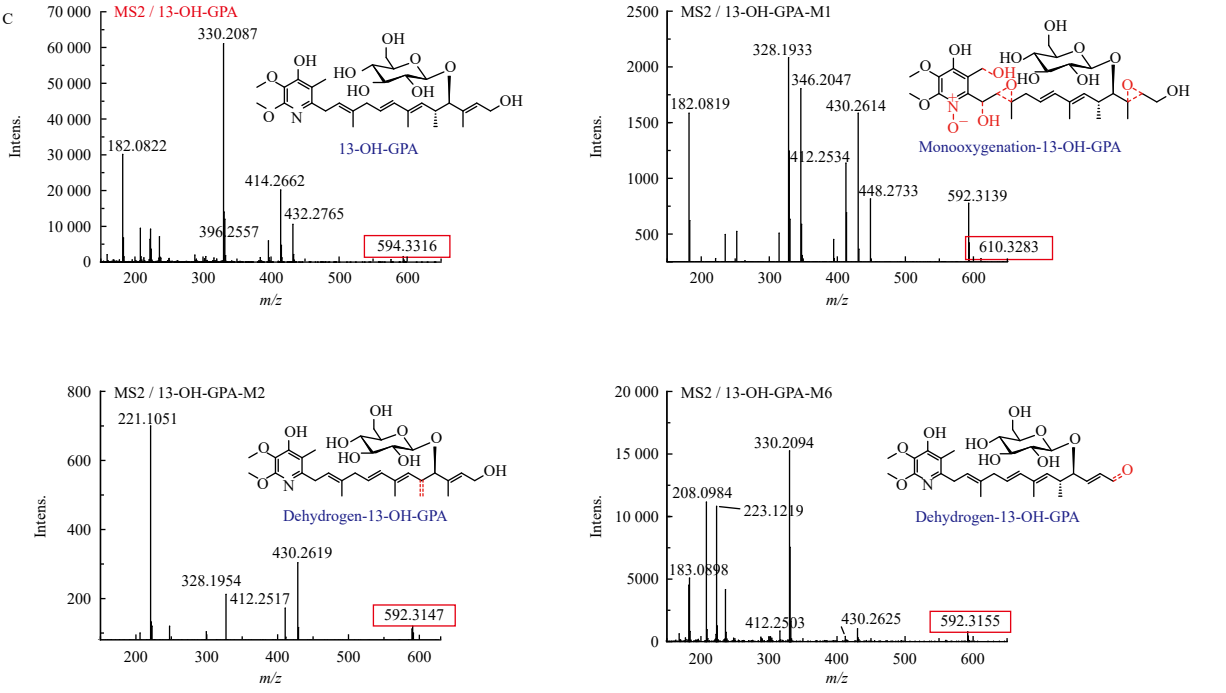

Fig. 4 MS2 spectrum (ESI$^+$, [M + H]$^+$) and corresponding chemical structures of the PA/GPA/13-OH-GPA and their major CYP metabolites after incubation with the microsomes. (A) MS2 spectrum and chemical structures of PA, dioxygenation-PA (M1), monooxygenation-PA (M2), and dehydrogenation-PA (M8). (B) MS2 spectrum and chemical structures of GPA, dioxygenation-GPA (M1), monooxygenation-GPA (M6), and dehydrogenation-GPA (M7). (C) MS2 spectrum and chemical structures of 13-OH-GPA, monooxygenation-13-OH-GPA (M1) and dehydrogen-13-OH-GPA (M2, M6).

more pronounced than in other enzymes. However, PA and GPAs demonstrated substantial differences in metabolism among the UGTs. The prototype elimination rates of UGT1A7, UGT1A8, UGT1A9, and UGT1A10 were significant, ranging from 30% to 70% (Figs. 9D–9F). No notable prototype elimination was observed for the remaining metabolic enzymes. Comparatively, the prototype elimination rates of UGTs were considerably higher than those of CYPs, suggesting that metabolism was primarily mediated by UGTs. Thus, UGT1A7, UGT1A8, UGT1A9, and UGT1A10 were identified as the main metabolic enzymes responsible for the metabolism of PA, GPA, and 13-OH-GPA, with UGT1A7 contributing most significantly to the metabolic process.

2.6. Toxicity

Throughout the administration period, the mice maintained normal activity and mental status, with no significant variations in body weight across groups (Fig. 10A). To assess the potential toxicity of GPAs on the primary metabolic organs, liver and kidneys, plasma levels of biochemical indicators of liver and kidney function —alanine aminotransferase (ALT), aspartate aminotransferase (AST), and creatinine (CRE) —were measured, and liver and kidney sections were subjected to hematoxylin-eosin (HE) staining. The results revealed no significant differences in ALT, AST, and CRE levels among the groups (Fig. 10B). HE staining demonstrated that both liver and kidney tissues maintained structural integrity, exhibiting orderly cellular arrangement without apparent inflammatory cell infiltration (Fig. 10C). In conclusion, continuous gavage administration of PA, GPA, and 13-OH-GPA at efficacy doses did not induce hepatorenal toxicity in mice.

2.7. Effects on the activity of CYPs

Following seven days of oral administration in mice, the activity of each metabolic enzyme was quantified by measuring the formation of corresponding metabolites (nmol·mg^{-1}·min^{-1}). Fig. 11 illustrates the key enzyme activity of CYPs in liver microsomes. Table S1 details the optimization conditions for probe substrate metabolites, while Figure S5 presents the standard curves. Compared to the control group, the PA group showed decreased formation rates of acetaminophen (APAP) and 4-OH-diclofenac (DIC) by 10.7% and 49.3%, respectively, while the formation rate of 6-OH-Testosterone (TES) increased by 24.1%. The GPA and 13-OH-GPA groups exhibited increased formation rates of 4-OH-DIC by 39.7% and 52.6%, respectively, and 4-OH-Mephenytoin (MP) by 164.9% and 122.3%, respectively. Additionally, all candidate drugs increased the formation rates of dextromethorphan (DM) and dextrorphan (DXO) by 30%–130% and decreased the formation rate of 6-OH-Chlorzoxazone (CLZ) by 8%–21%. These results demonstrate that PA and GPAs significantly affect CYP activity after seven days of oral administration. Notably, GPA and 13-OH-GPA consistently display synchronous inhibition or induction of metabolic enzymes, suggesting a strong correlation between their glycoside structure and their impact on metabolic enzyme activity.

3. Discussion

Despite its low bioavailability, 13-OH-GPA demonstrated higher distribution in the kidney compared to PA and GPA, contributing to its favorable pharmacological effects in the target organ. To enhance oral bioavailability, potential modification of the hydroxyl group at C-13 of 13-OH-GPA may reduce UGT-mediated biotransformation and improve the compound's druggability.

The pharmacokinetic profiles of orally administered drugs revealed that PA and GPAs were swiftly absorbed and eliminated in mice, exhibiting short half-lives. Notably, a significant correlation emerged between the absorption and elimination of the drugs and the structural variations among the three candidate compounds. In contrast to the aglycone PA, glycosylation enhanced the absorption of GPA in the gastrointestinal tract, resulting in an earlier T_{max} from the initial 30 min to 10 min. Moreover, with the additional incorporation of a hydroxyl group, 13-OH-GPA achieved peak concentration in as little as 2 min. Furthermore, the $MRT_{0\text{-}t}$ of GPA and 13-OH-GPA were lower than that of PA, indicating a more rapid elimination rate *in vivo* for the two

Table 2 High-resolution mass-spectrum data of PA/GPA/13-OH-GPA and their CYPs and UGTs-mediated metabolites after incubation with RLMs and HLMs.

Metabolite	RT(min)	$[M+H]^+$ (*m/z*)	Smart Formula [M]	Major fragment ions	Identification
PA	20.2	416.2787	$C_{25}H_{37}NO_4$	398, 332, 208, 182	**PA**
M1	11.0	448.2667	$C_{25}H_{37}NO_6$	430, 412, 314, 182	Dioxygenation-PA
M2	14.9	432.2722	$C_{25}H_{37}NO_5$	414, 396, 332, 182	Monooxygenation-PA
M3	15.5	432.2719	$C_{25}H_{37}NO_5$	414, 396, 330, 182	Monooxygenation-PA
M4	15.9	432.2786	$C_{25}H_{37}NO_5$	414, 396, 332, 182	Monooxygenation-PA
M5	16.5	432.2709	$C_{25}H_{37}NO_5$	414, 396, 330, 182	Monooxygenation-PA
M6	17.2	432.2758	$C_{25}H_{37}NO_5$	414, 332, 208, 182	Monooxygenation-PA
M7	17.9	432.2725	$C_{25}H_{37}NO_5$	414, 396, 330, 182	Monooxygenation-PA
M8	20.6	414.2635	$C_{25}H_{35}NO_4$	396, 332, 208, 182	Dehydrogen-PA
PA-Glu1	13.0	592.3128	$C_{31}H_{45}NO_{10}$	416, 398, 332, 182	PA-glucuronide1
PA-Glu2	13.3	592.3151	$C_{31}H_{45}NO_{10}$	416, 398, 332, 182	PA-glucuronide2
GPA	14.8	578.3339	$C_{31}H_{47}NO_9$	416, 398, 332, 182	**GPA**
M1	9.0	610.3245	$C_{31}H_{47}NO_{11}$	592, 448, 430, 412	Dioxygenation-GPA
M2	9.4	610.3240	$C_{31}H_{47}NO_{11}$	592, 448, 430, 412	Dioxygenation-GPA
M3	10.0	610.3274	$C_{31}H_{47}NO_{11}$	592, 448, 430, 412	Dioxygenation-GPA
M4	10.2	610.3283	$C_{31}H_{47}NO_{11}$	592, 448, 430, 412	Dioxygenation-GPA
M5	10.4	610.3183	$C_{31}H_{47}NO_{11}$	592, 448, 430, 412	Dioxygenation-GPA
M6	11.6	594.3309	$C_{31}H_{47}NO_{10}$	432, 414, 330, 182	Monooxygenation-GPA
M7	12.0	576.3189	$C_{31}H_{45}NO_9$	414, 396, 330, 221	Dehydrogen-GPA
M8	12.1	594.3325	$C_{31}H_{47}NO_{10}$	432, 414, 396, 182	Monooxygenation-GPA
GPA-Glu	10.1	754.3663	$C_{37}H_{55}NO_{15}$	578, 416, 398, 332	GPA-glucuronide
13-OH-GPA	11.6	594.3316	$C_{31}H_{47}NO_{10}$	432, 414, 396, 330	**13-OH-GPA**
M1	9.0	610.3283	$C_{31}H_{47}NO_{11}$	592, 448, 430, 412	Monooxygenation-13-OH-GPA
M2	9.5	592.3147	$C_{31}H_{45}NO_{10}$	430, 412, 328, 221	Dehydrogen-13-OH-GPA
M3	9.9	610.3246	$C_{31}H_{47}NO_{11}$	592, 448, 430, 412	Monooxygenation-13-OH-GPA
M4	10.2	610.3194	$C_{31}H_{47}NO_{11}$	592, 448, 430, 412	Monooxygenation-13-OH-GPA
M5	11.0	610.3236	$C_{31}H_{47}NO_{11}$	592, 448, 412, 330	Monooxygenation-13-OH-GPA
M6	12.0	592.3155	$C_{31}H_{45}NO_{10}$	430, 412, 330, 208	Dehydrogen-13-OH-GPA
13-OH-GPA-Glu1	8.2	770.3638	$C_{37}H_{55}NO_{16}$	594, 432, 414, 330	13-OH-GPA-glucuronide1
13-OH-GPA-Glu2	8.9	770.3601	$C_{37}H_{55}NO_{16}$	608, 432, 414, 330	13-OH-GPA-glucuronide2

glycosides compared to the aglycone. Consequently, the presence of glycosides and hydroxyl groups in the structure significantly accelerated both the absorption rate (13-OH-GPA > GPA > PA) and elimination rate of the drugs, aligning with previously reported findings [20,21].

In contrast, during the pharmacokinetic study of intravenous administration, mice receiving PA at an equivalent dose to other groups experienced mortality due to PA's potent mitochondrial respiratory inhibitory effect upon entering the blood circulation. This severe toxicity evidently results in suboptimal drug properties for PA. However, intravenous administration of the two glycosides did not elicit significant toxicity, indicating a substantial reduction in the extreme toxicity of aglycone through glycoside introduction. Further comparison of the pharmacokinetic properties of the two glycosides upon intravenous administration reveals that 13-OH-GPA exhibited lower $MRT_{0\text{-}t}$ and $T_{1/2}$ values than GPA, while its CL was greater, suggesting a faster *in vivo* elimination rate for 13-OH-GPA compared to GPA. These findings indicate that the introduction of a hydroxyl group to glycosides can accelerate the drug's clearance rate. In summary, the structural specificity of the three candidate drugs significantly influences their absorption, elimination, and toxicity profiles. Calculations reveal that the oral bioavailability of GPA and 13-OH-GPA was notably low, at only 5.06% and 2.69%, respectively.

In tissue distribution studies, PA and GPAs exhibited notably high distribution in the liver (50%–79%), with PA reaching up to 79.0%. This tendency for PA to accumulate in the liver, a non-target organ, may lead to adverse effects and potential toxicity. Importantly, the introduction of glycosides significantly mitigates PA's propensity for liver accumulation. Conversely, if the drug's distribution site aligns with its pharmacologically active site, it may function as a drug reservoir, potentially extending the duration of action. Although 13-OH-GPA demonstrated low oral bioavailability, its distribution in the kidney (19.8%) exceeded that of PA (10.0%) and GPA (7.3%). Building on previous research [6], 13-OH-GPA exhibited rapid and sustained activation of the LKB1/AMPK signaling pathway in renal tubular cells, potentially delaying renal fibrosis and AKI. In contrast, the structurally similar PA failed to induce LKB1 activation, showing insignificant anti-AKI activity. Studies have reported that hydroxyl-modified

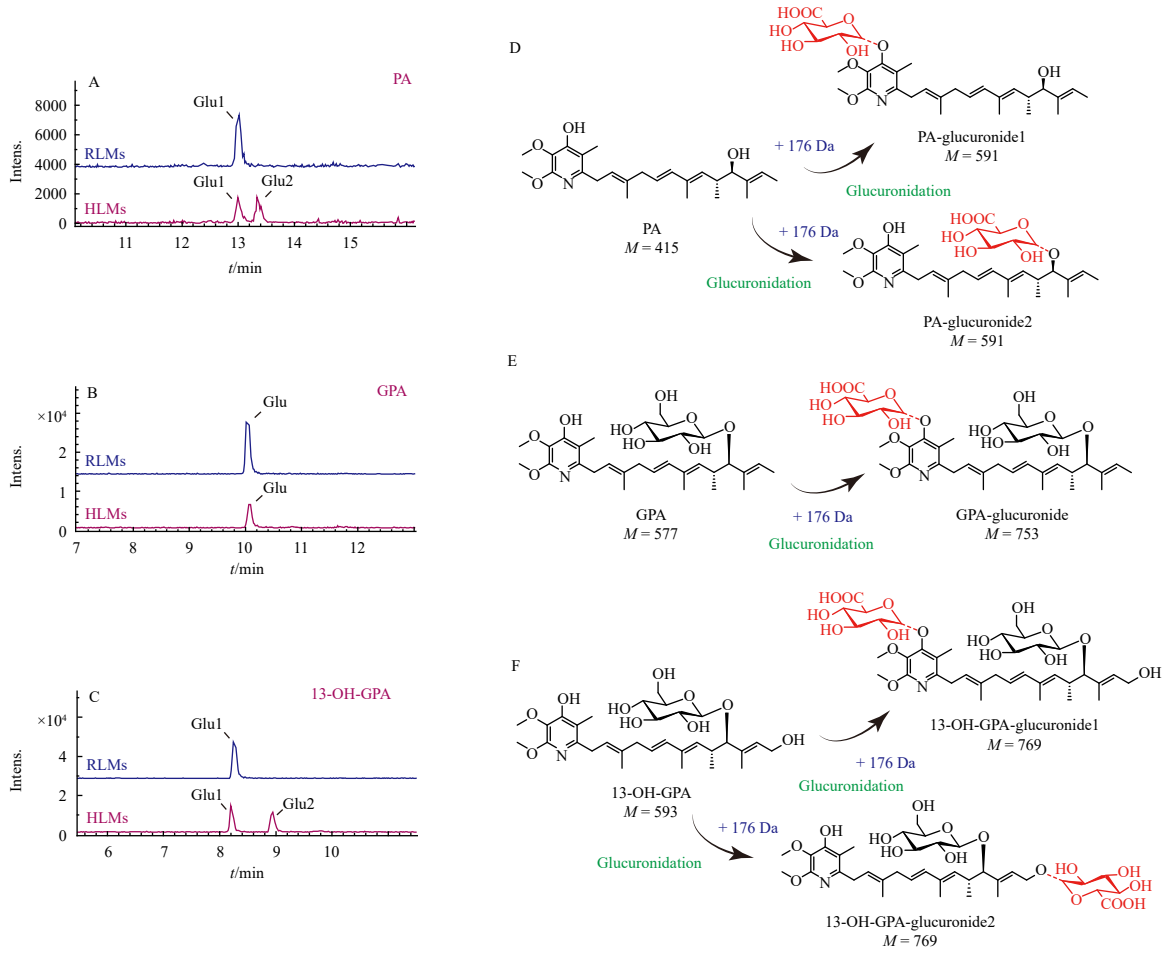

Fig. 5 Identification of the glucuronidation metabolites of PA/GPA/13-OH-GPA in RLMs and HLMs. (A, D) Total ion flow chromatograms of PA (10 μmol·L^{-1}) after glucuronidation in microsomes and the proposed metabolic pathways. One glucuronide of PA (PA-Glu1) was identified in RLMs, and two glucuronides of PA (PA-Glu1 and PA-Glu2) were identified in HLMs. (B, E) Total ion flow chromatograms of GPA (10 μmol·L^{-1}) after glucuronidation in microsomes and the proposed metabolic pathways. Only one glucuronide product of GPA (GPA-Glu) was identified in both RLMs and HLMs. (C, F) Total ion flow chromatograms of 13-OH-GPA (10 μmol·L^{-1}) after glucuronidation in microsomes and the proposed metabolic pathways. One glucuronide of 13-OH-GPA was identified in RLMs, and two glucuronides of 13-OH-GPA (13-OH-GPA-Glu1 and 13-OH-GPA-Glu2) were identified in HLMs.

polymers can advantageously accumulate in damaged kidneys due to their excellent hydrophilicity, enhancing their potential as renal drug delivery carriers for AKI therapy [22]. Thus, the superior renal distribution of 13-OH-GPA may contribute to its enhanced biological effects in the target organ.

The significant first-pass effect, primarily involving metabolism mediated by CYPs and UGTs, is a key factor contributing to the low oral bioavailability of most drugs [23-26]. Consequently, the low bioavailability of GPA and 13-OH-GPA may also be attributed to this rapid metabolic process. The high affinity of PA and GPAs for the liver facilitates their metabolic modification. Furthermore, PA and GPAs demonstrate substantial CYP- and UGT-mediated metabolic instability in HLMs. Various metabolic products, including monooxygenation, dioxygenation, dehydrogenation, and glucuronidation derivatives, were isolated and identified in RLMs/HLMs. Notably, compared to CYP-mediated metabolism (prototype elimination rate < 20%), glucuronidation contributes more significantly to the clearance of PA and GPAs. The elimination rates by UGT1A7, UGT1A8, UGT1A9, and UGT1A10, the primary UGT enzymes responsible for PA and GPA metabolism, range from 30% to 70%. These enzymes are predominantly expressed in the intestines and liver. These findings suggest that PA and GPAs undergo rapid metabolic processes mediated by CYPs and UGTs in the liver and intestines before entering the circulatory system. The intense glucuronidation, in particular, may substantially contribute to the low oral bioavailability of GPA and 13-OH-GPA.

Of particular note is the low bioavailability of 13-OH-GPA, coupled with its significant renal distribution. This phenomenon can be attributed to the hydroxylation modification of 13-OH-GPA. The hydroxylation at the C-13 position serves as a target for glucuronidation, facilitating metabolism mediated by UGTs. Extensive biotransformation prior to drug absorption results in the lower bioavailability of 13-OH-GPA. Additionally, hydroxylation increases the polarity of 13-OH-GPA, enhancing its propensity for renal distribution and excretion, thus explaining its higher proportion in the kidney. In summary, the hydroxylation modification of 13-OH-GPA alters its absorption, distribution, and metabolism, collectively contributing to its reduced bioavailability and increased renal distribution.

The analysis indicates that while 13-OH-GPA's oral bioavailability is approximately half that of GPA, its distribution ratio in the kidney is more than double. This suggests that if the challenge of low oral bioavailability can be addressed, 13-OH-GPA could emerge as a promising candidate for kidney disease treatment. Structural modifications, particularly the introduction of hydroxyl functions, significantly influence oral bioavailability [27]. As previously noted, glucuronidation of 13-OH-GPA primarily occurs at the C-4' phenolic hydroxyl group on the pyridine ring and the C13 hydroxyl group, which is the primary cause of its UGT-mediated metabolic instability. These findings suggest that strategic optimization of the hydroxyl group might reduce the rapid biotransformation of 13-OH-GPA and enhance its bioavailability. Given that the C-4' phenolic hydroxyl group on the pyridine ring

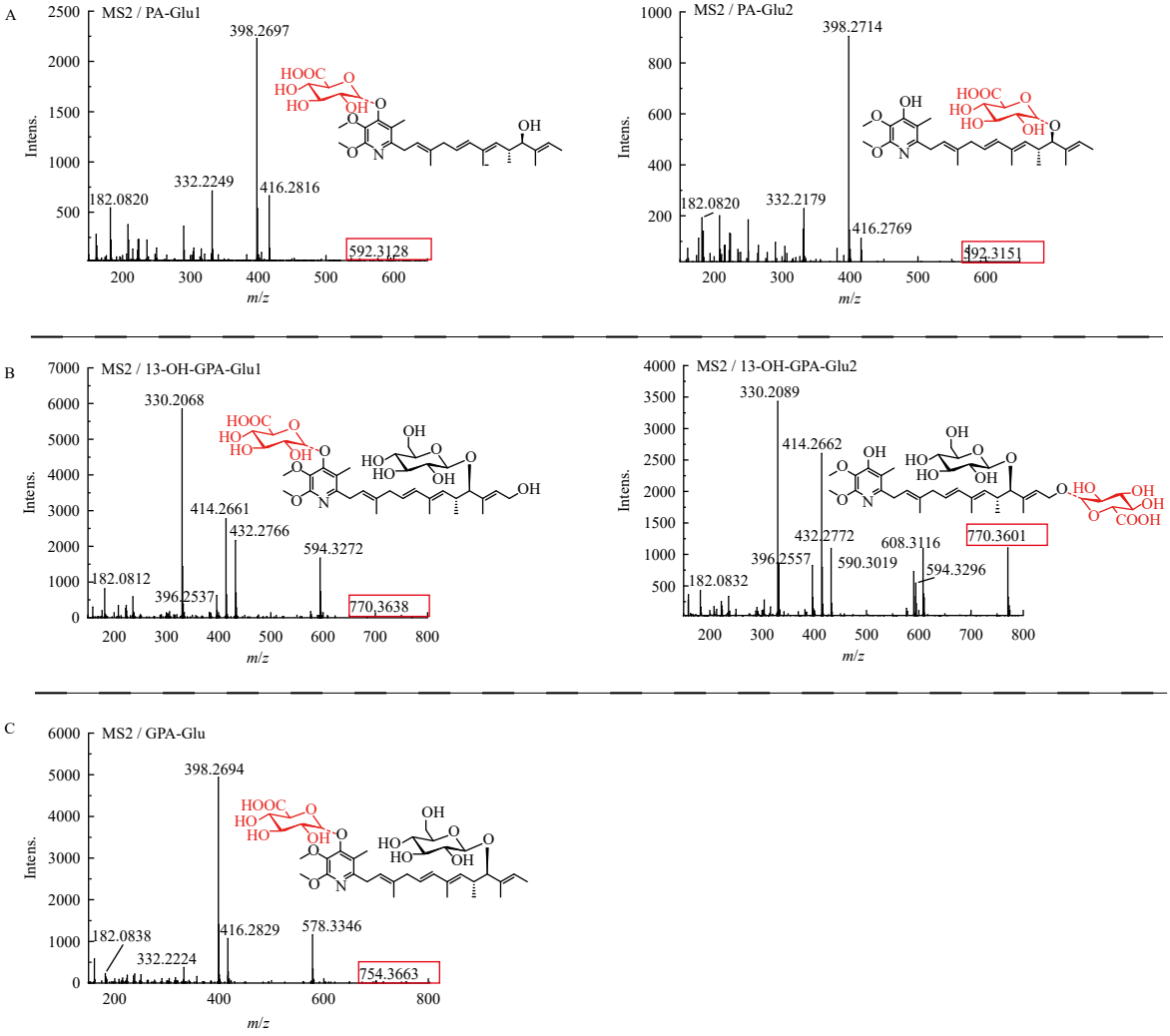

Fig. 6 MS2 spectrum (ESI$^+$, $[M + H]^+$) of the glucuronides of the PA/GPA/13-OH-GPA and corresponding chemical structures after incubation with the microsomes. (A) MS2 spectrum and chemical structures of PA-glucuronide1 and PA-glucuronide2. (B) MS2 spectrum and chemical structures of 13-OH-GPA-glucuronide1 and 13-OH-GPA-glucuronide2. (C) MS2 spectrum and chemical structure of GPA-glucuronide.

is essential for maintaining high activity [28, 29], a more viable approach would involve modifying the C-13 hydroxyl group in 13-OH-GPA into a more stable structure. This modification could potentially reduce biotransformation, improve metabolic stability, and increase oral bioavailability.

This study revealed that exposure to PA and GPAs significantly influenced the activity of several key CYPs, particularly CYP2C9, CYP2C19, CYP2D6, and CYP2E1, in addition to their own metabolic characteristics. This finding indicates a potential risk of CYP-mediated DDIs. Both PA and GPAs exhibited inhibitory effects on CYP2E1 enzyme activity to varying degrees. CYP2E1 is known to metabolize various exogenous drugs and small-molecule carcinogens, including APAP, isoniazid, alcohol, toxins, and carcinogenic precursors, which can lead to hepatorenal toxicity or the bioactivation of carcinogenic metabolites [30]. Consequently, the selective inhibition of CYP2E1 enzyme activity by PA and GPAs may have potential significance in mitigating exogenous toxicity and reducing tumor susceptibility [31, 32]. Conversely, GPA and 13-OH-GPA significantly induced the enzyme activity of CYP2C9, CYP2C19, and CYP2D6. These enzymes are primary metabolic enzymes for numerous antidepressants, antipsychotics, and antihypertensive drugs, such as amitriptyline, fluoxetine, and metoprolol [33, 34]. A reported clinical adverse reaction case suggested that cabozantinib might have a clinically significant drug interaction as a mixed inhibitor of CYP2C9 and 2C19 when combined with warfarin [35]. Similarly, the induction of these metabolic enzymes following GPA and 13-OH-GPA administration may accelerate the elimination of relevant drugs, potentially resulting in decreased plasma concentrations and diminished drug efficacy. Furthermore, this study identified various oxidation products, dehydrogenation products, and glucuronidation products of PA and GPAs. Numerous studies have reported that drugs and their metabolites can jointly affect the activity of metabolic enzymes, suggesting a high risk of metabolite-mediated drug interactions [36-38]. Therefore, when administering PA and GPAs in combination with other medications, careful attention should be given to the potential occurrence of adverse effects caused by DDIs to ensure medication safety.

In recent decades, numerous ADME/T prediction platforms leveraging computer technology have been developed to assist researchers in comprehensively evaluating potential drug candidates [39, 40]. These platforms serve as powerful tools for understanding the pharmacological properties of drug candidates and guiding structure optimization. The prediction results are presented in Table S2. Upon comparison, some experimental data were successfully predicted. For instance, PA was anticipated to undergo metabolic reactions mediated by both CYPs and UGTs, which aligns with our findings identifying various metabolites produced by these enzymes. However, discrepancies exist between certain experimental data and predicted results, such as bioavailability, CL and $T_{1/2}$, and substrate/inhibitor status of CYPs. These indicators may be influenced by factors including animal species [41-43], drug dose dependence [44], and *in vivo* conditions, resulting in outcomes that differ from predictions. Notably, the predic-

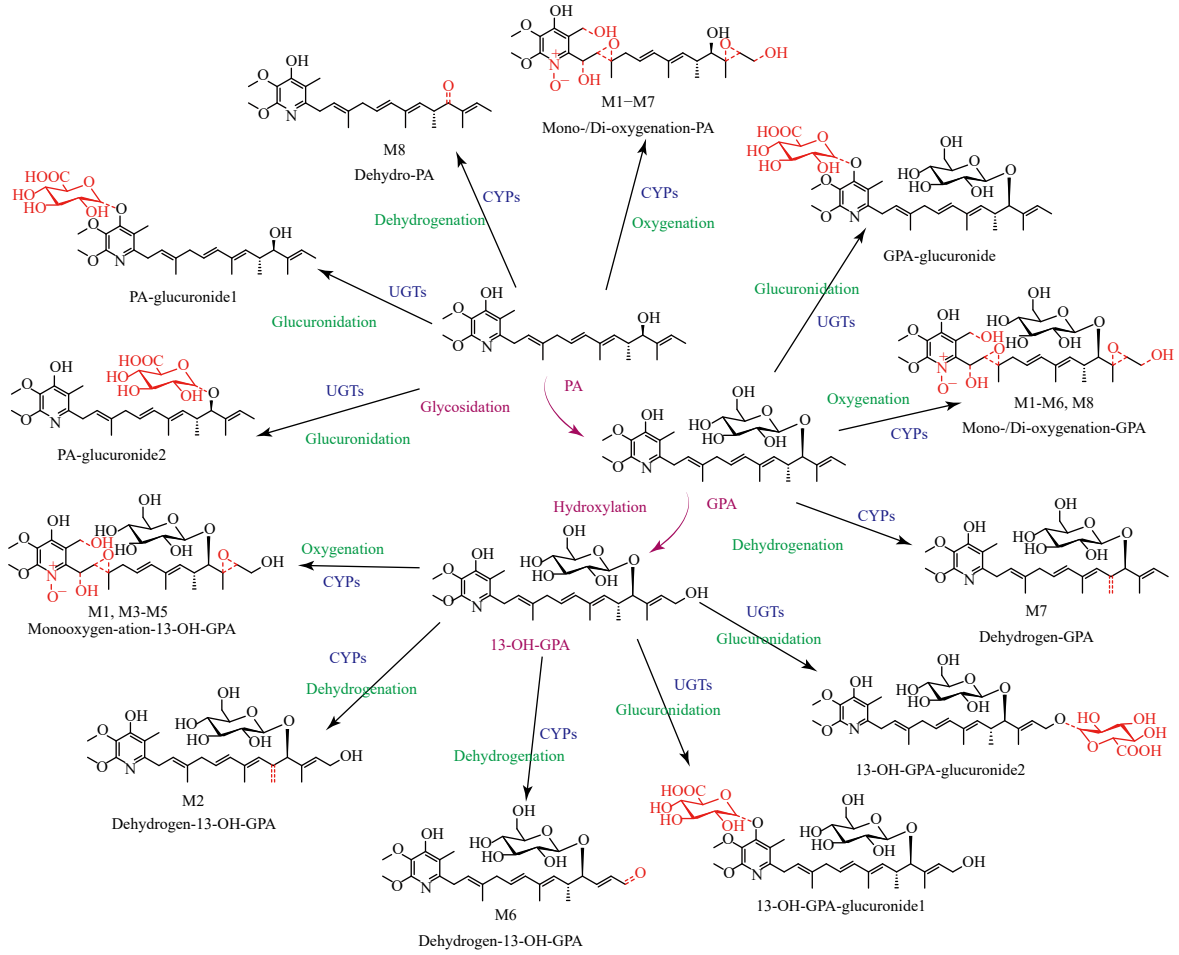

Fig. 7 Proposed metabolic pathways of PA/GPA/13-OH-GPA in RLMs and HLMs.

tion results suggest that PA and GPAs may also undergo sulfonation reactions. Structurally, various hydroxyl groups could serve as potential sites for sulfonation. Consequently, PA and GPAs may be subject to CYP- and UGT-mediated metabolism as well as sulfonation metabolism, potentially contributing to the low bioavailability of GPAs. However, further experimental studies are necessary to validate this hypothesis.

4. Conclusion

In summary, this study systematically elucidated the pharmacokinetic characteristics and metabolic profiles of PA and its glycosides (GPA, 13-OH-GPA). The biopharmaceutical properties of PA and GPAs were closely related to the structural features of the candidate drugs themselves. Rapid and extensive glucuronidation emerged as the primary pathway for the elimination of PA and GPAs, potentially contributing to their low oral bioavailability. Structural optimization or development of renal-targeted agents of 13-OH-GPA to reduce biotransformation and enhance bioavailability presents promising prospects. Furthermore, PA and GPAs significantly influenced the activity of key CYPs. Given the variety of CYP-mediated metabolites identified, further experimental evaluation is warranted to investigate potential DDI mechanisms induced by these metabolites. This paper aims to provide new insights into the relationship between the structure and efficacy of natural piericidins from a biopharmaceutical perspective by comprehensively characterizing their metabolic properties. Overall, this study provides a solid theoretical basis for the structural optimization and safe use of marine-derived piericidins as candidate drugs for the treatment of kidney disease.

5. Materials and methods

5.1. Chemicals and reagents

PA, GPA, and 13-OH-GPA were previously isolated, purified, and identified by Xuefeng Zhou's group, as reported in earlier literature. The compounds, determined to be > 95% pure by HPLC analysis, were stored at −20 °C until use and dissolved in DMSO. Pooled HLMs were obtained from Corning Incorporated (NY, USA). The recombinant human CYP isoforms (CYP1A2, CYP2B6, CYP2C9, CYP2C19, CYP2D6, CYP3A4, CYP4F2, and CYP4A11) and the recombinant human UGT isoforms (UGT1A1, UGT1A3, UGT1A4, UGT1A6, UGT1A7, UGT1A8, UGT1A9, UGT1A10, UGT2B4, UGT2B7, UGT2B15, and UGT2B17) were purchased from Cypex (Scotland, UK). The NADPH regeneration system (solution A and solution B) for the CYP assay was acquired from Promega (Madison, USA). Uridine diphosphate glucuronic acid (UDPGA) was obtained from Sigma-Aldrich (MO, USA). TES, alamethicin, saccharolactone, magnesium chloride ($MgCl_2$), potassium phosphate dibasic (K_2HPO_4), potassium dihydrogen phosphate (KH_2PO_4), sucrose and ethylenediaminetetraacetic acid dipotassium salt (EDTA·K_2·$2H_2O$) were purchased from Aladdin (Shanghai, China). CLP (IS) was obtained from Meilun-Bio (Liaoning, China). 6-OH-TES was purchased from Apexbio (CZT, USA). PH, DIC, DM, DXO, APAP, CLZ, Verapamil (VER, IS), dithiothreitol (DTT), and phenyl methanesulfonyl fluoride (PMSF) were obtained from Yuanye Bio-Technology Co., Ltd (Shanghai, China). MP was purchased from GLPBIO (CA, USA). 4-OH-MP was purchased from TRC (ON, Canada). 4-OH-DIC and 6-OH-CLZ were purchased from TLC (ON, Canada). All other chemicals were acquired from standard commercial sources of the

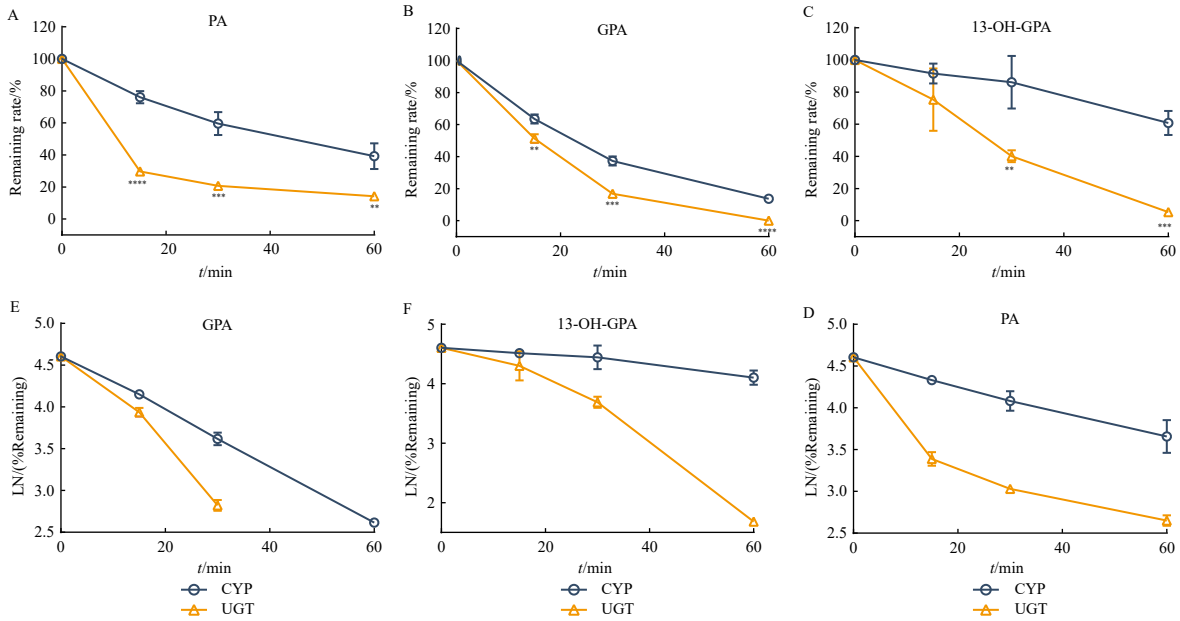

Fig. 8 Metabolic stability of PA/GPA/13-OH-GPA in HLMs *in vitro*. (A–C) CYPs- and UGTs-mediated and the time-dependent prototype remaining rate (%) of PA/GPA/13-OH-GPA (5 μmol·L^{-1}) in HLMs. (D–F) The natural log curve of the corresponding remaining percentage (LN%) versus incubation time (min). All the incubations were done in triplicate. Data are expressed as mean ± SD. $^{**}P$< 0.01, $^{***}P$ < 0.005, $^{****}P$ < 0.001 *vs* CYPs reaction at the same time point.

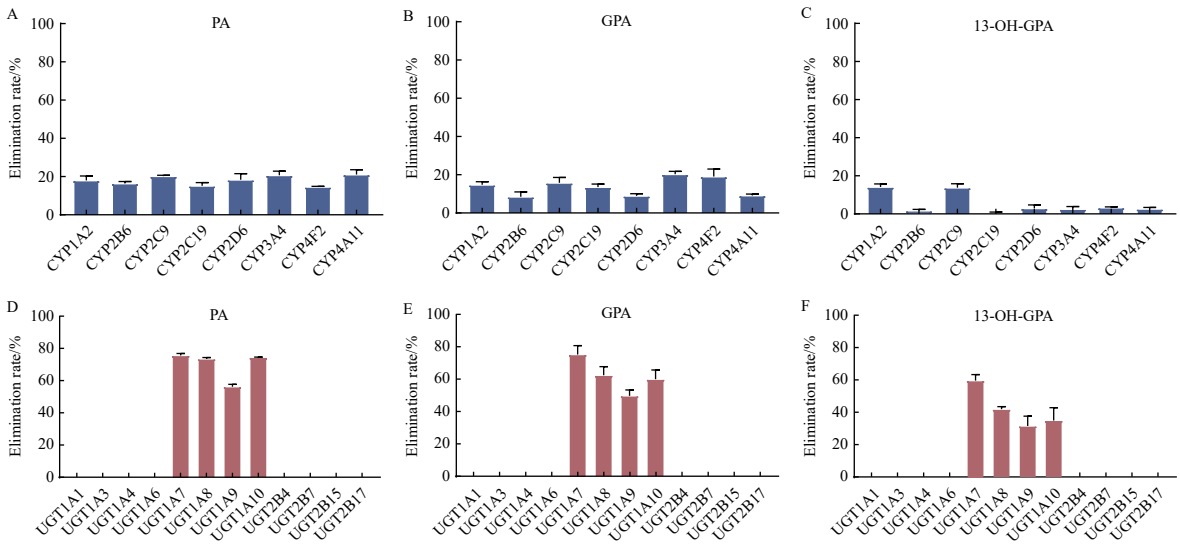

Fig. 9 Metabolic characterization of PA/GPA/13-OH-GPA (5 μmol·L^{-1}) in recombinant human enzymes. (A–C) Prototype elimination rate of PA/GPA/13-OH-GPA (5 μmol·L^{-1}) in eight recombinant human CYPs. (D–F) Prototype elimination rate of PA/GPA/13-OH-GPA (5 μmol·L^{-1}) in twelve recombinant human UGTs. All incubations were done in triplicate. Data are expressed as mean ± SD.

highest quality available.

5.2. Animals

Male C57BL mice (specific pathogen-free, 22–25 g) and male Sprague-Dawley rats (specific pathogen-free, 200–250 g) were acquired from Guangzhou Jinwei Biotechnology Co., Ltd. (Guangdong, China). The animals were provided unrestricted access to food and water and allowed to acclimate for one week under a 12-h light/dark cycle. All animal procedures were approved by the Animal Ethics Committee of Southern Medical University.

5.3. Analytical instruments and conditions

For the quantification of PA, GPA and 13-OH-GPA, the primary operational parameters were established as follows: system, LC-30AD (Shimadzu, Kyoto, Japan) coupled with a 4000 Q-Trap mass spectrometer (AB SCIEX, CA, USA); column, Waters ACQUITY UPLC BEH C18 1.7 μm; curtain gas, 35psi; ion spray voltage, 4500 V; temperature, 500 °C; ion source gas1 (GS1), 55 psi; ion source gas2 (GS2), 55psi. The mobile phase A comprised 0.1% formic acid and 2 mmol·L^{-1} ammonium formate in water, while mobile phase B consisted of 100% carbinol. The gradient was programmed as follows: 0–0.3 min, 0% to 20%B; 0.3–0.8 min, 20% to 95%B; 0.8–3.8 min, 95% to 95%B; 3.8–6.0 min, 95% to 20%B. The injection volume was 5 μL, with a total flow rate of 0.4 mL·min^{-1}. The MRM detection channels and compound-dependent parameters are presented in Table S1.

5.4. Method validation

The linearity, accuracy, and precision of the analytes were evaluated in plasma, tissue homogenates, and potassium phosphate buffer (KPI). The established calibration curves demonstrated high linearity, with R^2 values exceeding 0.993 (Fig. S6). The intra-day and inter-day precision remained within an accept-

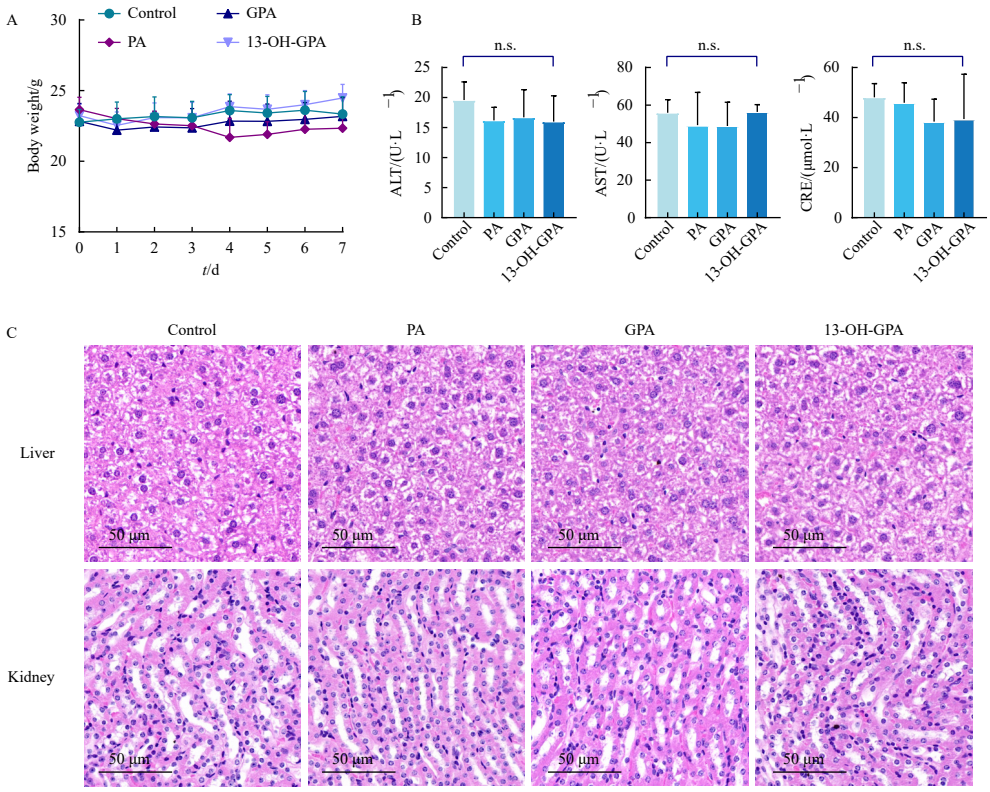

Fig. 10 Mice were intragastric administrated with PA/GPA/13-OH-GPA (2.5 mg·kg^{-1}) for seven days. (A) Changes in body weight of mice within different groups after being administrated with drug for seven days. (B) Biochemical analysis of ALT, AST, and CRE activities in plasma in mice after treatment. (C) Representative liver and kidney HE staining (original amplification, × 200) from control and PA/GPA/13-OH-GPA treated mice. All data are expressed as mean ± SD (n = 6). n.s. indicate no statistical significance compared to the control group.

able range of 15%, while the accuracy was maintained between 90% and 115% (Table S3), adhering to the standards for biological sample analysis. The analytes exhibited substantial stability after 2 h of incubation in KPI buffer solution at 37 °C (Table S4). In conclusion, the analytical method developed in this study satisfies the requirements for subsequent experiments.

5.5. Pharmacokinetics

Male C57BL mice (n = 5) were fasted for 12 h prior to the pharmacokinetic study. PA/GPA/13-OH-GPA were prepared in 0.5% methylcellulose suspensions and administered to mice *via* gavage at doses of 6/10/10 mg·kg^{-1}. For intravenous injection, PA/GPA/3-OH-GPA were initially dissolved in 30% PEG300, then diluted with physiological saline. These drugs were administered to mice through tail vein injection at doses of 0.8/2.0/2.0 mg·kg^{-1}, respectively. Blood samples (120–150 μL) were collected from the vein of the eye sockets. The samples were promptly centrifuged at 8000 r·min^{-1} for 8 min (4 °C). 50 μL plasma was combined with 200 μL methanol solvent containing testosterone (100 ng·mL^{-1}). After vortexing, the mixture was centrifuged (4 °C, 13000 r·min^{-1}, 20 min), and the supernatant was transferred to a new tube and dried under vacuum overnight. The resulting dried powder was reconstituted in a 1 : 1 mixture of methanol and water and then centrifuged for quantitative analysis.

5.6. Oral bioavailability

The oral bioavailability (F%) of the drug was calculated using the following formula:

$$F\% = \frac{AUC_{0\text{-t,p.o}} \times Dose_{i.v}}{AUC_{0\text{-t,i.v}} \times Dose_{p.o}} \times 100\%$$

In this formula, $AUC_{0\text{-t,p.o}}$ and $AUC_{0\text{-t,i.v}}$ denote the area under the concentration-time curve calculated following oral and intravenous administration, respectively. $Dose_{p.o}$ and $Dose_{i.v}$ indicate the respective doses administered orally and intravenously.

5.7. Distribution

Prior to the tissue distribution experiment, male C57BL mice (n = 5) were subjected to overnight fasting. PA (10 mg·kg^{-1}), GPA (10 mg·kg^{-1}), and 13-OH-GPA (10 mg·kg^{-1}) were administered to mice by gavage, respectively. At 30 min and 60 min post-administration, the mice were euthanized by cervical dislocation, and tissue samples were collected from the heart, liver, spleen, lung, and kidney. The tissue samples were thoroughly rinsed with physiological saline and blotted dry with filter paper before being homogenized in cold physiological saline (tissue : saline = 1 : 5). The tissue homogenate (100 μL) was spiked with a methanol solvent (400 μL) containing testosterone (100 ng·mL^{-1}). After thorough vortexing, the samples were centrifuged at 13000 r·min^{-1} for 20 min. The resulting supernatant was vacuum-dried overnight, redissolved, centrifuged, and subjected to quantitative analysis.

5.8. Preparation of RLMs

Male rats in good health were euthanized by extracting blood from the abdominal aorta. The liver was excised, washed in a cleaning solution (comprising 8 mmol·L^{-1} KH_2PO_4, 5.6 mmol·L^{-1} EDTA·K_2·$2H_2O$, 1mmol·L^{-1} DTT and 229.6 μmol·L^{-1} PMSF), sectioned into smaller fragments, and promptly homogenized in tissue buffer (containing 1.8 μmol·L^{-1} KH_2PO_4, 8 mmol·L^{-1} K_2HPO_4, 250 mmol·L^{-1} sucrose, 1 mmol·L^{-1} EDTA·K_2·$2H_2O$ and 229.6 μmol·L^{-1} PMSF). The resulting homogenate underwent centrifugation at 10400 r·min^{-1} and 4 °C for 15 min, followed by centrifugation of the supernatant at 35000 r·min^{-1} and 4 °C for 60 min.

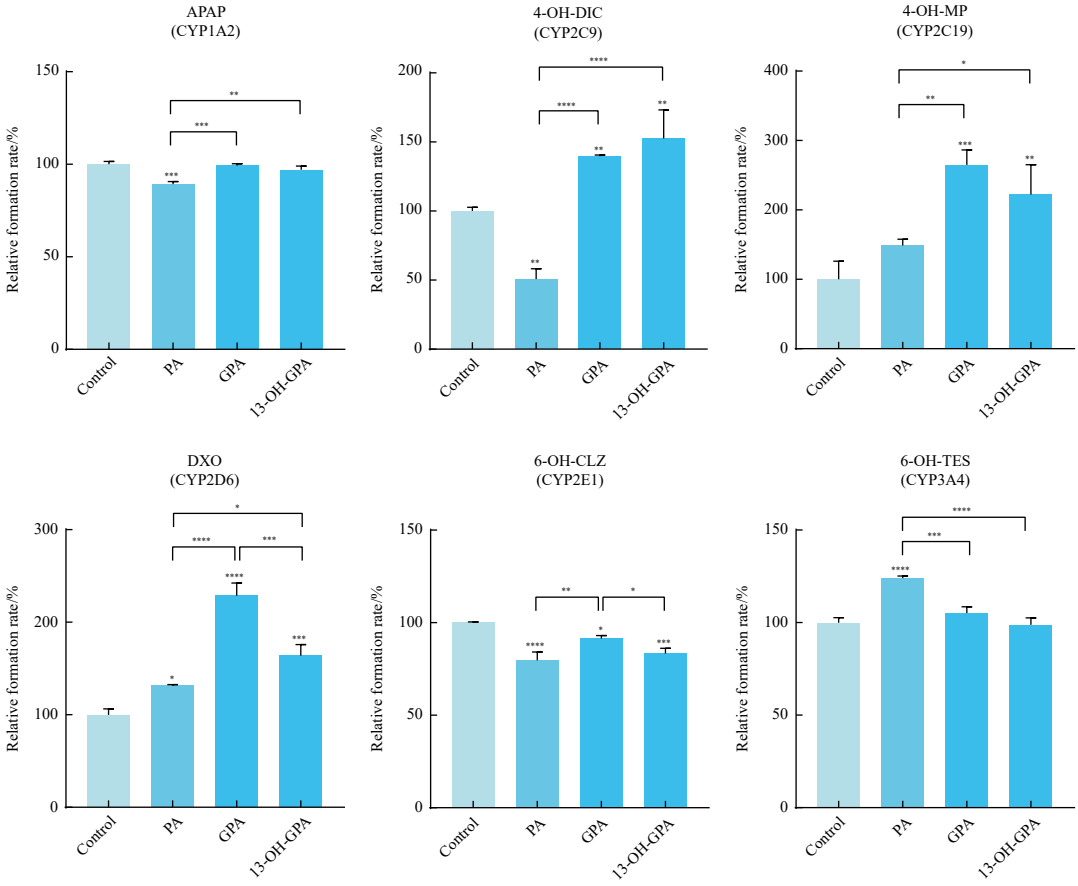

Fig. 11 The effect of PA/GPA/13-OH-GPA on the critical cytochrome P450 enzymes activities in the mice liver. All incubations were done in triplicate. Data are expressed as mean ± SD. $^{*}P < 0.05$, $^{**}P < 0.01$, $^{***}P < 0.005$, $^{****}P < 0.001$ *vs* the control group.

The precipitate was resuspended in a 250 mmol·L^{-1} sucrose solution. The prepared liver microsomes were stored at −80 °C. All procedures were conducted on ice.

5.9. Incubation systems in RLMs and HLMs

The typical CYPs incubation procedure was conducted as follows: 385 μL of 50 mmol·L^{-1} phosphate buffer (KPI, pH 7.4), 8 μL of RLMs or HLMs, and 4 μL of PA, GPA, or 13-OH-GPA were sequentially added to a 1.5 mL centrifuge tube. The incubation mixture underwent pre-incubation for 5 min at 37 °C. Subsequently, the reaction was initiated by adding 0.5 μL of Solution B and 2.5 μL of Solution A. The total system comprised 3.3 mmol·L^{-1} $MgCl_2$, 0.2 mg·mL^{-1} RLMs or HLMs, 3.3 mmol·L^{-1} glucose-6-phosphate, 0.4 U·mL^{-1} glucose-6-phosphate dehydrogenase, and 5 or 10 μmol·L^{-1} PA, GPA, or 13-OH-GPA. The reaction system was then incubated in a 37 °C water bath for 60 min.

The UGT incubation process was similar for all compounds. In a 1.5 mL centrifuge tube, 250 μL of 50 mmol·L^{-1} KPI phosphate buffer, 70 μL of Solution B, 20 μL of RLMs or HLMs, 4 μL of PA/GPA/13-OH-GPA, and 56 μL of Solution A were combined. The specific UGTs incubation mixture contained 5 mmol·L^{-1} $MgCl_2$, 0.2 mg·mL^{-1} RLMs or HLMs, 0.125 mg·mL^{-1} alamethicin, 5.25 mg·mL^{-1} saccharolactone, and 5 or 10 μmol·L^{-1} PA/GPA/13-OH-GPA. The mixtures were then incubated for 30 min.

To terminate the reaction, 200 μL of ice-cold methanol containing testosterone (5 μmol·L^{-1}) was added. The mixture was then centrifuged at 13000 r·min^{-1} for 20 minutes. Subsequently, the supernatants were analyzed using LC-MS/MS for quantification. All reactions were performed in triplicate.

5.10. Identification of metabolites

Metabolite identification was conducted using a liquid chromatograph (Agilent 1260, CA, USA) coupled with a quadrupole time-of-flight (Q-TOF) high-definition mass spectrometer (Bruker maXis, MA, Germany). The specific conditions and instrument parameters were as follows: column, Luna 5u C_{18} (2) 100 A 150*4.60 mm 5 micro; capillary, 4500 V (ESI^+); end plate offset, 500 V; nebulizer, 1.0 bar; dry gas, 6.0 L·min^{-1}; dry temperature, 180 °C; scan range, 100–2000 *m/z*. The mobile phase composition was as previously described, with the following elution gradient: 0 min, 20% B; 0–10 min, 20% to 70% B; 10–20 min, 70% to 100%B; 20–25 min, 100% to 100% B; 25–25.1 min, 100% to 20% B; 25.1–30 min, 20% to 20% B. The injection volume was 60 μL, with a total flow rate of 1 mL·min^{-1}.

5.11. Assay for metabolic stability in HLMs

HLMs at a final concentration of 0.2 mg·mL^{-1} were utilized for both CYP and UGT reactions. Samples of 100 μL were extracted from the reaction system at 0, 15, 30, and 60 minutes post-incubation, with the reaction halted by the addition of an internal standard. The residual rates at each time point were quantified using liquid chromatography-tandem mass spectrometry (LC-MS/MS). Subsequently, a natural logarithm curve of the residual percentage (LN%) against incubation time (min) was constructed, and the intrinsic clearance (CL_{int}) *in vivo* was calculated according to established methodologies [45, 46].

$$T_{1/2} = \frac{0.693}{k}$$

$$CL_{int}(in\ vivo) = \frac{0.693}{T_{1/2}(in\ vitro)} \times \frac{\text{mL incubation}}{\text{mg microsomes}} \times \frac{45\ \text{mg microsomes}}{\text{g liver}} \times \frac{20\ \text{g liver}}{\text{kg boby weight}}$$

In the formula, k denotes the slope of the natural logarithmic curve representing the percentage of residues (LN%) of PA and GPAs in the reaction mixture as a function of incubation time (min).

5.12. Metabolism in recombinant human CYP and UGT isoforms

The incubation of PA/GPA/13-OH-GPA (5 μmol·L^{-1}) with microsomes containing eight recombinant human CYP isoforms (CYP1A2, CYP2B6, CYP2C9, CYP2C19, CYP2D6, CYP3A4, CYP4F2 and CYP4A11) and twelve recombinant human UGT isoforms (UGT1A1, UGT1A3, UGT1A4, UGT1A6, UGT1A7, UGT1A8, UGT1A9, UGT1A10, UGT2B4, UGT2B7, UGT2B15 and UGT2B17) followed the same procedure as previously described for microsomes. The only modification was the final enzyme concentration, which was adjusted to 20 ng·mL^{-1}. All experiments were conducted in triplicate.

5.13. Activity of CYPs in mouse liver microsomes (MLMs)

Mice were administered PA/GPA/13-OH-GPA at 2.5 mg·kg^{-1} *via* gavage for seven consecutive days. On the eighth day, MLMs were prepared according to the protocol described in item 5.8, with a final concentration of 0.2 mg·mL^{-1}. The probe substrates and their corresponding metabolic enzymes were utilized as follows: Phenacetine (PH, 1 μmol·L^{-1}) for CYP1A2, DIC (1 μmol·L^{-1}) for CYP2C9, MP (450 μmol·L^{-1}) for CYP2C19, DM (1 μmol·L^{-1}) for CYP2D6, CLZ (10 μmol·L^{-1}) for CYP2E1, and TES (1 μmol·L^{-1}) for CYP3A4. The reaction was terminated using frozen methanol containing VER (20 ng·mL^{-1}) in ESI$^+$ mode or CLP (200 ng·mL^{-1}) in ESI$^-$ mode. The probe substrates and their corresponding metabolites were as follows: PH/APAP, DIC/4-OH-DIC, MP/4-OH-MP, DM/DXO, CLZ/6-OH-CLZ, TES/6-OH-TES. All experiments were conducted in triplicate.

5.14. Data analysis

Pharmacokinetic parameters were calculated using DAS 2.0 software, employing a standard non-compartmental method. All data are presented as mean ± standard deviation. Statistical differences were evaluated using Student's t-test or one-way ANOVA analysis conducted with GraphPad Prism 8.0. A *P*-value of < 0.05 was considered to indicate a statistically significant difference.

Funding

This work was supported by the Special Project for Marine Economic Development of Department of Natural Resources of Guangdong Province (No. GDNRC[2024]25), National Natural Science Foundation of China (Nos. 82274002, U20A20101), Guangdong Local Innovation Team Program (No.2019BT02Y262), Science and Technology Innovation Project of Guangdong Medical Products Administration (Nos.S2021ZDZ042, 2023ZDZ06, 2024-ZDZ08, 2024A1515012477).

Supporting Information

The supplementary information mainly include MS2 spectra of all CYP metabolites, comparison of GPA-M6 and 13-OH-GPA, methodological validation, and comparison of AMDE/T predictions and actual results.

Declaration of Competing Interest

The authors have declared no conflicts of interest.

References

1 Carroll AR, Copp BR, Davis RA, et al. Marine natural products. *Nat Prod Rep*. 2023;40(2):275-325. https://doi.org/10.1039/D2NP00083K.
2 A MAG, C MATB, E EDD, et al. Insights about clinically approved and preclinically investigated marine natural products. *Curr Res Biotechnol*. 2020;2:88-102. https://doi.org/10.1016/j.crbiot.2020.09.001.
3 Li K, Liang Z, Chen W, et al. Iakyricidins A–D, antiproliferative piericidin analogues bearing a carbonyl group or cyclic skeleton from Streptomyces iakyrus SCSIO NS104. *J Org Chem*. 2019;84(19):12626-12631. https://doi.org/10.1021/acs.joc.9b01270.
4 Li K, Su Z, Gao Y, et al. Cytotoxic minor piericidin derivatives from the actinomycete strain Streptomyces psammoticus SCSIO NS126. *Mar Drugs*. 2021;19(8).
5 Zhou X, Liang Z, Li K, et al. Exploring the natural piericidins as anti-renal cell carcinoma agents targeting peroxiredoxin 1. *J Med Chem*. 2019;62(15):7058-7069. https://doi.org/10.1021/acs.jmedchem.9b00598.
6 Liu C, Wang X, Wang X, et al. A new LKB1 activator, piericidin analogue S14, retards renal fibrosis through promoting autophagy and mitochondrial homeostasis in renal tubular epithelial cells. *Theranostics*. 2022;12(16):7158-7179. https://doi.org/10.7150/thno.78376.
7 Liang Z, Chen Y, Gu T, et al. LXR-mediated regulation of marine-derived piericidins aggravates high-cholesterol diet-induced cholesterol metabolism disorder in mice. *J Med Chem*. 2021;64(14):9943-9959. https://doi.org/10.1021/acs.jmedchem.1c00175.
8 Xiao Z, Morris-Natschke SL, Lee KH. Strategies for the optimization of natural leads to anticancer drugs or drug candidates. *Med Res Rev*. 2016;36(1):32-91. https://doi.org/10.1002/med.21377.
9 Hodgson J. ADMET-turning chemicals into drugs. *Nat Biotechnol*. 2001;19(8):722-726. https://doi.org/10.1038/90761.
10 Tsaioun K, Jacewicz M. De-risking drug discovery with ADDME -- avoiding drug development mistakes early. *Altern Lab Anim*. 2009;37 Suppl 1:47-55.
11 Knights KM, Stresser DM, Miners JO, et al. *In vitro* drug metabolism using liver microsomes. *Curr Protoc Pharmacol*. 2016;74:7.8. 1-7.8. 24.
12 Wu Y, Pan L, Chen Z, et al. Metabolite identification in the preclinical and clinical phase of drug development. *Curr Drug Metab*. 2021;22(11):838-857. https://doi.org/10.2174/1389200222666211006104502.
13 Han J, Gong S, Bian X, et al. Polarity-regulated derivatization-assisted LC-MS method for amino-containing metabolites profiling in gastric cancer. *J Pharm Anal*. 2023;13(11):1353-1364. https://doi.org/10.1016/j.jpha.2023.06.009.
14 Zhang J, Chen Q, Zhang L, et al. Simultaneously quantifying hundreds of acylcarnitines in multiple biological matrices within ten minutes using ultrahigh-performance liquid-chromatography and tandem mass spectrometry. *J Pharm Anal*. 2024;14(1):140-148. https://doi.org/10.1016/j.jpha.2023.10.004.
15 Manikandan P, Nagini S. Cytochrome P450 structure, function and clinical significance: A Review. *Curr Drug Targets*. 2018;19(1):38-54.
16 Sun L, Mi K, Hou Y, et al. Pharmacokinetic and pharmacodynamic drug-drug interactions: research methods and applications. *Metabolites*. 2023;13(8):897. https://doi.org/10.3390/metabo13080897.
17 Matsumoto M, Mogi K, Nagaoka K, et al. New piericidin glucosides, glucopiericidins A and B. *J Antibiot (Tokyo)*. 1987;40(2):149-156. https://doi.org/10.7164/antibiotics.40.149.
18 Morita K, Kato M, Kudo T, et al. *In vitro-in vivo* extrapolation of metabolic clearance using human liver microsomes: factors showing variability and their normalization. *Xenobiotica*. 2020;50(9):1064-1075. https://doi.org/10.1080/00498254.2020.1738592.
19 Pelkonen O, Turpeinen M. *In vitro-in vivo* extrapolation of hepatic clearance: biological tools, scaling factors, model assumptions and correct concentrations. *Xenobiotica*. 2007;37(10-11):1066-1089. https://doi.org/10.1080/00498250701620726.
20 Pan W, Xue B, Yang C, et al. Biopharmaceutical characters and bioavailability improving strategies of ginsenosides. *Fitoterapia*. 2018;129:272-282. https://doi.org/10.1016/j.fitote.2018.06.001.
21 Manach C, Scalbert A, Morand C, et al. Polyphenols: food sources and bioavailability. *Am J Clin Nutr*. 2004;79(5):727-747. https://doi.org/10.1093/ajcn/79.5.727.
22 Haque N, Parveen S, Tang T, et al. Marine natural products in clinical use. *Mar Drugs*. 2022;20(8).
23 Kang HE, Cho YK, Jung HY, et al. Pharmacokinetics and first-pass effects of liquiritigenin in rats: low bioavailability is primarily due to extensive gastrointestinal first-pass effect. *Xenobiotica*. 2009;39(6):465-475. https://doi.org/10.1080/00498250902890151.
24 Matsuda Y, Konno Y, Hashimoto T, et al. Quantitative assessment of intestinal first-pass metabolism of oral drugs using portal-vein cannulated rats. *Pharm Res*. 2015;32(2):604-616. https://doi.org/10.1007/s11095-014-1489-x.
25 Xie L, Diao Z, Xia J, et al. Comprehensive evaluation of metabolism and the contribution of the hepatic first-pass effect in the bioavailability of glabridin in rats. *J Agric Food Chem*. 2023;71(4):1944-1956. https://doi.org/10.1021/acs.jafc.2c06460.
26 Zhao C, Ying Z, Hao D, et al. Investigating the bioavailabilities of olerciamide A via the rat's hepatic, gastric and intestinal first-pass effect models. *Biopharm Drug Dispos*. 2019;40(3-4):112-120. https://doi.org/10.1002/bdd.2175.
27 Cramer J, Sager CP, Ernst B. Hydroxyl groups in synthetic and natural-

product-derived therapeutics: a perspective on a common functional group. *J Med Chem*. 2019;62(20):8915-8930. https://doi.org/10.1021/acs.jmedchem.9b00179.
28 Zhou X, Fenical W. The unique chemistry and biology of the piericidins. *J Antibiot (Tokyo)*. 2016;69(8):582-593. https://doi.org/10.1038/ja.2016.71.
29 Miyoshi H. Structure-activity relationships of some complex I inhibitors. *Biochim Biophys Acta*. 1998;1364(2):236-244. https://doi.org/10.1016/S0005-2728(98)00030-9.
30 Chen J, Jiang S, Wang J, et al. A comprehensive review of cytochrome P450 2E1 for xenobiotic metabolism. *Drug Metab Rev*. 2019;51(2):178-195. https://doi.org/10.1080/03602532.2019.1632889.
31 Monostory K, Hazai E, Vereczkey L. Inhibition of cytochrome P450 enzymes participating in p-nitrophenol hydroxylation by drugs known as CYP2E1 inhibitors. *Chem Biol Interact*. 2004;147(3):331-340. https://doi.org/10.1016/j.cbi.2004.03.003.
32 Trafalis DT, Panteli ES, Grivas A, et al. CYP2E1 and risk of chemically mediated cancers. *Expert Opin Drug Metab Toxicol*. 2010;6(3):307-319. https://doi.org/10.1517/17425250903540238.
33 Rodríguez Arcas MJ, García-Jiménez E, Martínez-Martínez F, et al. Role of CYP450 in pharmacokinetics and pharmacogenetics of antihypertensive drugs. *Farm Hosp*. 2011;35(2):84-92. https://doi.org/10.1016/j.farma.2010.05.006.
34 Zobdeh F, Eremenko II, Akan MA, et al. Pharmacogenetics and pain treatment with a focus on non-steroidal anti-inflammatory drugs (NSAIDs) and antidepressants: a systematic review. *Pharmaceutics*. 2022;14(6): 1190. https://doi.org/10.3390/pharmaceutics14061190.
35 Foxx-Lupo WT, Sing S, Alwan L, et al. A drug interaction between cabozantinib and warfarin in a patient with renal cell carcinoma. *Clin Genitourin Cancer*. 2016;14(1):e119-121. https://doi.org/10.1016/j.clgc.2015.09.015.
36 Ghassabian S, Gillani TB, Rawling T, et al. Sorafenib N-oxide is an inhibitor of human hepatic CYP3A4. *Aaps j*. 2019;21(2):15. https://doi.org/10.1208/s12248-018-0262-1.
37 Murray M, Gillani TB, Rawling T, et al. Inhibition of hepatic CYP2D6 by the active N-oxide metabolite of sorafenib. *Aaps j*. 2019;21(6):107. https://doi.org/10.1208/s12248-019-0374-2.
38 Xu Y, Xia Y, Liu Q, et al. Glutaredoxin-1 alleviates acetaminophen-induced liver injury by decreasing its toxic metabolites. *J Pharm Anal*. 2023;13(12):1548-1561. https://doi.org/10.1016/j.jpha.2023.08.004.
39 Xiong G, Wu Z, Yi J, et al. ADMETlab 2.0: an integrated online platform for accurate and comprehensive predictions of ADMET properties. *Nucleic Acids Res*. 2021;49(W1):W5-w14. https://doi.org/10.1093/nar/gkab255.
40 Djoumbou-Feunang Y, Fiamoncini J, Gil-de-la-Fuente A, et al. BioTransformer: a comprehensive computational tool for small molecule metabolism prediction and metabolite identification. *J Cheminform*. 2019;11(1):2. https://doi.org/10.1186/s13321-018-0324-5.
41 Lin JH. Species similarities and differences in pharmacokinetics. *Drug Metab Dispos*. 1995;23(10):1008-1021. https://doi.org/10.1016/S0090-9556(25)06742-X.
42 Martignoni M, Groothuis GM, de Kanter R. Species differences between mouse, rat, dog, monkey and human CYP-mediated drug metabolism, inhibition and induction. *Expert Opin Drug Metab Toxicol*. 2006;2(6):875-894. https://doi.org/10.1517/17425255.2.6.875.
43 Toutain PL, Ferran A, Bousquet-Mélou A. Species differences in pharmacokinetics and pharmacodynamics. *Handb Exp Pharmacol*. 2010; 199 (199):19-48.
44 Zamir A, Hussain I, Ur Rehman A, et al. Clinical pharmacokinetics of metoprolol: a systematic review. *Clin Pharmacokinet*. 2022;61(8):1095-1114. https://doi.org/10.1007/s40262-022-01145-y.
45 Manda VK, Avula B, Ali Z, et al. Evaluation of *in vitro* absorption, distribution, metabolism, and excretion (ADME) properties of mitragynine, 7-hydroxymitragynine, and mitraphylline. *Planta Med*. 2014;80(7):568-576. https://doi.org/10.1055/s-0034-1368444.
46 Manda VK, Avula B, Ali Z, et al. Characterization of *in vitro* ADME properties of diosgenin and dioscin from *Dioscorea villosa*. *Planta Med*. 2013;79(15):1421-1428. https://doi.org/10.1055/s-0033-1350699.